

# Holistic structure of neural pathways underlies brain perceptual rivalry: A physical perspective of auditory stream segregation

Yuxuan Wu<sup>1</sup>, Jinling Gao<sup>2</sup>, Xiaona Fang<sup>3\*</sup> and Jin Wang<sup>4\*</sup>

<sup>1</sup> Biophysics & Complex System Center, Center of Theoretical Physics, College of Physics, Jilin University, Changchun 130012, People's Republic of China

<sup>2</sup> State Key Lab of Superhard Materials, College of Physics, Jilin University, Changchun, 130012, China

<sup>3</sup> School of chemistry, Northeast Normal University, Changchun, Jilin, 130024, China

<sup>4</sup> Department of Chemistry and of Physics and Astronomy, Stony Brook University, Stony Brook, New York 11794, United States

\*Corresponding author: Jin Wang, Xiaona Fang

& 1 & 2 contributed equally to this work and should be considered co-first authors.

Email: [jin.wang.1@stonybrook.edu](mailto:jin.wang.1@stonybrook.edu), [Fangxn482@nenu.edu.cn](mailto:Fangxn482@nenu.edu.cn)

## Abstract

Understanding the brain perceptual functions as emerging from complex neural connections, rather than only the behavior of specific neural groups, is increasingly recognized today. Taking the auditory stream segregation, a classical issue in the field of perceptual behaviors, as an example, we demonstrate its emergence from the topological structure of neural pathways, by constructing a holistic neural circuit model based solely on existing neurophysiological data. Combining quantification of deterministic neural dynamics, potential landscape and probability flux, this model accurately reproduces the nonequilibrium phase transition process from integrated stream to completely segregated streams. The mean duration time (MDT) of the auditory perceptions from the simulation accords with the reported experimental results, and its inverse Gaussian distribution is suggested to complement the original Gamma or Lognormal distributions of the MDT. Further, using average probability flux and entropy production rate, we reveal the dynamical and thermodynamical origins, and the cost of the auditory phase transition process, highlighting the role of time irreversibility and detailed balance breaking as bridges between theory and neurophysiological experiment. Moreover, we propose a fundamental principle for attentional modulation and successfully apply this theoretical framework to an attention-modulated system. Finally, two psychoacoustic experiments are conducted to validate the constructed model and the proposed attention mechanism. Our results highlight that the neural basis of a perceptual and cognitive behavior is not limited to a localized brain neural region, but has a holistic and systematic origin.

## Introduction

It has been nearly 120 years since Korbinian Brodmann with his colleague introduce “area partition” into brain research. In the field of neuroscience, the concept that different nuclei or cortices perform their respective functions has gradually won support among researchers. whereas, increasing evidence ushers people comprehending cerebral neurophysiological function as the holistic, systematic and emergent behavior, in which complex connections among neurons play a significant role (1-5). This functional entirety is also found in brain perceptual behaviors: For binocular rivalry, a wide range of visual pathways are involved besides the primary visual cortex V1 (6, 7). Also, some reports indicate the increasing separation of auditory streams along the ascending auditory pathway (8). Going a step further, it is wondered that if the holistic structure itself of connections among neurons contains the mechanism of the perceptions, provided conforming to the reality of neurophysiology as much as possible.

We confirm the above hypothesis by establishing a biophysical model for auditory stream segregation, which is an epitome of auditory scene analysis and cocktail party problem, also a crucial element of the issue of perceptual rivalry. “auditory stream” refers to the perceptual organization of individual sound sequences (9-11). Studies primarily utilize the paradigm and its derivative of presenting listeners with a repeating ABA\_ triplet tones

auditory sequence, and analyzing the reported auditory perceptions of the listeners (12-17). Following the initial organization of auditory streams, listeners typically experience three distinct perceptual phases: (1) Only integrated stream that continuous ABA\_ sequence is perceived, (2) “auditory bistability” or “ambiguous perception” involving alternation between integrated stream and A\_A\_A\_ or B\_\_B\_\_ sequences, and (3) exclusive alternation between segregated streams A\_A\_A\_ and B\_\_B\_\_ as the foreground and background respectively (18). The distinction among the auditory scene components leads to their grouping into separate streams. For the ABA\_ paradigm, increasing the frequency difference  $\Delta f$  between A and B tones from zero causes the occurrence of these three phases sequentially and continuously.

Despite numerous experimental findings over the years, opinions vary on the underlying neural mechanism and dynamics of the auditory stream segregation. Various models, such as those based on the abstract neural network (13, 19), models based on the organization of events and chains (14, 15), models based on Gestalt psychology (20), and other studies (21-24) have demonstrated feasibility from different perspectives, reproducing experimental results under specific conditions. From the perspective of holistic function of neural connections, leveraging advancements in neurophysiology, we sort out and organize the entire auditory neural circuit encompassing of ascending and descending auditory pathways, from which a topological structure is extracted to form a neural circuit model. It possesses three characteristics: (1) adherence to known results in neurophysiological anatomy, avoiding abstract or phenomenological artificial structure, (2) systematic reflection of the entire neural circuit, instead of localizing in regional structures such as the cochlea or primary auditory cortex, and (3) no additional assumptions on the dynamical mechanism beyond the sigmoidal function of stimulus-feedback, neural adaptation, and modulation of  $\Delta f$  and attention.

Building upon our model, we employ nonlinear stochastic dynamics to unveil the underlying dynamical structure of the auditory stream integration and segregation, and display the stochastic switch between those auditory perceptions (25). Above this, nonequilibrium potential landscape from the global steady probability distribution and the probability flux as the driving force for nonequilibrium phase transitions are quantified. (26). Along with  $\Delta f$  as an order parameter, two bifurcations or nonequilibrium phase transitions emerges amid phase transition process in the deterministic dynamical structure and the nonequilibrium potential landscape, by which three dynamical phases *Integration*, *Rivalry* and *Segregation* are separated that sequentially replicate the aforementioned three auditory phases. Notably, our finding suggests that empirical *Segregation* phase is the continuation of *Rivalry* phase, while the integrated perception is the inherent intermediation between the foreground and background segregated perceptions. Results of dominant path obtained by the stochastic path integral method determine the dynamical path of the switching between perceptual states, also the intermediating role of integrated perception (27, 28). Next, combining the landscape and the stochastic simulation, we quantify the mean duration time (MDT) of the auditory perceptions under different  $\Delta f$  and inspect its corresponding dynamics. The results accurately match the reported experiments. For the MDT distribution, we suggest the inverse Gaussian distribution as a complement for the lognormal or gamma distribution. Particularly,  $\Delta f = 0.6$  in our model, at which MDTs of the integrated and segregated perceptions are proximate, is pinned down as an anchor point connecting with five semitones in the experiments (13, 14). This contributes to subsequent research.

Recent years have witnessed a surge in interest regarding the energy and cost of the brain and even the auditory system (29-31). Our framework extends beyond dynamics to analyze the entire auditory stream phase transition process through the lens of nonequilibrium thermodynamics. Our results demonstrate that average nonequilibrium probability steady-state flux ( $ave \mathbf{J}_{ss}$ ) and entropy production rate (*EPR*) reveal the dynamical and thermodynamical origins of the critical phase transition (32-34). Especially, our results show that in terms of thermodynamics although the system exhibits completely segregated auditory streams when  $\Delta f$  is large, the *Rivalry* and *Segregation* phases form a cohesive entirety as a phase transition process, aligning with the deterministic dynamics. Interestingly, the maximum values of  $ave \mathbf{J}_{ss}$  and *EPR* occurs at  $\Delta f = 0.55$ , contiguous to but before  $\Delta f = 0.6$  due to the landscape structure. All these characteristics are reflected in the difference between forward and backward cross-correlations  $\Delta_{corr}$ , which represents the time irreversibility or degree of detailed balance breaking (35-37). Most significantly, the  $\Delta_{corr}$  calculated from finite time series data serves as a prospective bridge connecting the theory and experiment, as such data can be yielded through various invasive or non-invasive brain experimental methods, as discussed in the main content.

Those results above are finally applied to analyze the model regulated by the attention, which is an inevitable factor in the auditory streams segregation process (38-41). We first propose a fundamental principle that

simultaneous amplification or attenuation of attentions on A, B tones will shorten or lengthen the  $\Delta f$  range required for the entire phase transition process. Based on this, simulation results confirm the reported experimental consequence that tilting of the attentions causes the corresponding shifts in the weights of auditory perceptions (41, 42). *EPR* results show that the minimum cost precisely appears at equal attentions that is closer to equilibrium, while a system with tilted attentions incurs greater cost. This provides a systematic explanation of neural adaptation. Significantly, although  $\Delta f$  changes, amplifying or abating the attentions appropriately can replicate the *EPR* situation of  $\Delta f = 0.55$  with attentions at balance level. This echoes our previous results of dynamics and thermodynamics, highlighting the complementarity between  $\Delta f$  and the attentions.

Two psychoacoustical experiments are carried out and their findings are interpreted in this study. Our first experiment validates the theoretical predication that the integrated perception intermediates the switching between the foreground and background segregated streams, supporting the rationality of the underlying dynamical structure revealed by our model. The second experiment validates that different degrees of listener distraction result in varying increments in the weight of the integrated perception, reinforcing our findings on the attention mechanism. Collectively, these results underscore the potential of a systematic, holistic, and physical approach to deciphering auditory stream segregation.

## Results

### Dynamical model of the entire auditory neural circuit and frequency-dependent landscapes

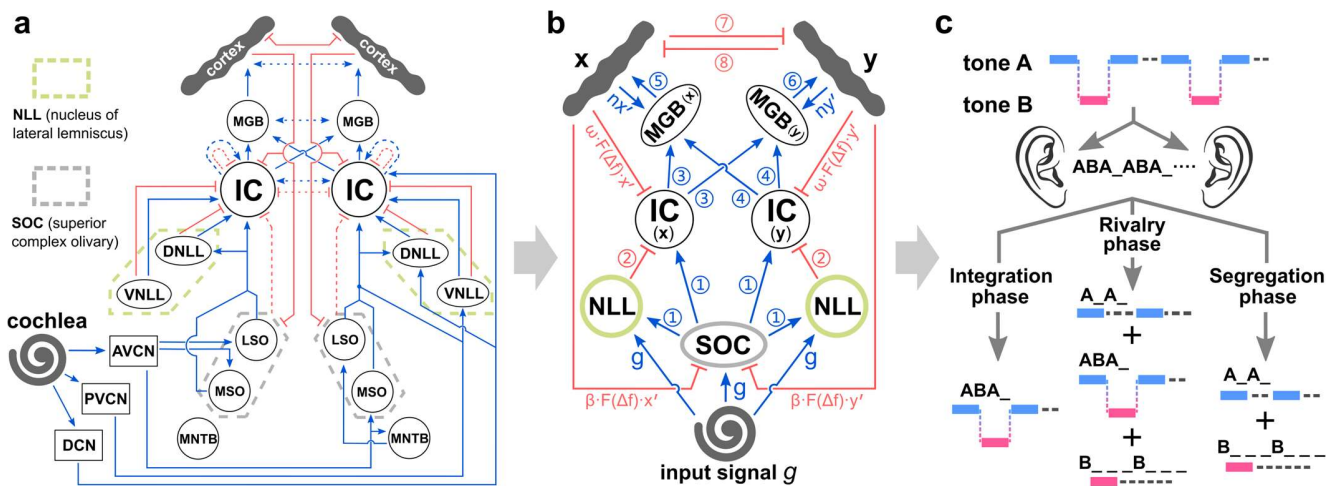


**FIG.1. a:** The auditory neural feedback pathways that may contribute to the auditory stream segregation and auditory scene analysis. Abbreviations of the pathway components are explained in main text. Only one side of the binaural pathways is displayed. Blue arrows represent the excitatory auditory neural pathways, while red bars represent the inhibitory ones. Dash lines represent the pathways which are not ascertained or not effective to the auditory stream segregation. **b:** The entire auditory neural circuit model after abstraction. The serial numbers and components beside pathways correspond to those in Eq.(1). **c:** Illustration for the auditory stream segregation.

The previously identified auditory neural feedback pathways that implicate in the auditory stream segregation is delineated as shown in Fig.1(a) (43-48). This network comprises ascending (centripetal) pathways primarily dedicating to signal transmission through excitation, and descending (centrifugal) pathways generally exerting inhibitory control for finer modulation. For ascending pathways that mainly conveys the signal towards the superior neural hierarchies, the external signal is captured by the cochlea, then transmitted to the anteroventral cochlear nucleus (AVCN), dorsal cochlear nucleus (DCN), and posteroventral cochlear nucleus (PVCN). With signals being decoded in the cochlea, the frequency-specific neural fibers are projected and mapped into the cochlear nucleus, where rudimentary streams for binaural sound localization and sound identification can be already detected (49). Subsequently, one part of signals projects to the lateral superior olivary nucleus (LSO), medial superior olivary nucleus (MSO), and medial nucleus of the trapezoid body (MNTB), while another part directly reaches the dorsal nucleus of the lateral lemniscus (DNLL) and ventral nucleus of the lateral lemniscus (VNLL). Generally, they are scaled as the superior olivary complex (SOC) and the nucleus of lateral lemniscus (NLL). NLL processes the

information of sound localization and time-variant frequency spectrum (50-52). The continuously ascending neural impulse excites the DNLL again and the superior neural hierarchy, inferior colliculus (IC). The ascending pathways and signals converge in the IC and are partially processed. These signals, after being processed by the medial geniculate body (MGB) that is grouped together as a functional unit with the cortex, access the cortex ultimately.

Descending pathways originate primarily from the auditory cortex, projecting to the NLL and the SOC (43, 46), which regulate the frequency processing (53). This regulation implies a strong correlation between the inhibitory feedbacks and the frequency. Notably, the inhibition in the cortex itself relates not only to frequency but also to attention modulation (54-58). Besides, NLL serves as a principal source of inhibition projection to the IC, in which the VNLL is instrumental to the pattern of cross-frequency interaction (59, 60), while the DNLL enhances the lateralization of the sound (43). In the IC, a highly intricate interplay effectuates the frequency selectivity and the temporal sensitivity. It is confirmed that this interaction involves the multilateral input of excitation and inhibition, as well as the exquisite interaction between the internal neural laminae in the IC of each side, although the latter is not fully understood (43). However, it appears that the inhibitory projections from other neural groups can be mapped in the IC (43).

Based on the result of Fig.1(a), the model of the entire auditory neural circuit is derived (Fig.1(b)).  $x$ ,  $y$  represent the firing rate of the neural populations in the auditory cortex, corresponding to excitations for different sound frequencies respectively, which positions are not fixed in the cortex (albeit there may be cortical spatial correlation (61)). The mutual excitations reflect the entirety of the cortex and the MGB. Between  $x$  and  $y$ , the mutual inhibition occurs respecting the attention  $I_x$ ,  $I_y$ , and the function  $F(\Delta f) = \ln[1 + (\Delta f/v)]$  of the frequency difference  $\Delta f$  of the input sound signal, in which the logarithm is employed to assure the slowly variation at large  $\Delta f$  values under the effect of critical band for a certain frequency (9). Also, the modulations by  $F(\Delta f)$  appear within the cortical inhibitions to the IC and SOC. Due to the mapped neural projections into the IC, the asymmetric inhibition to the IC is rational, whereas the direct and cross input from the IC to the MGB maintains the symmetric ascending pathways. In our model, we set the input signal as a constant  $g$ , and every ascending signals as the elementary sigmoidal functions without further stronger hypotheses, reading

$$\begin{aligned}
① \quad & F_{SOC} = \alpha[1 + \tanh(g - \beta F(\Delta f)(x' + y'))] \\
② \quad & F_{NLL} = \eta[1 + \tanh(g + F_{SOC})] \\
③ \quad & F_{IC}^x = \gamma[1 + \tanh(F_{SOC} - F_{NLL} - \omega F(\Delta f)x')] \\
④ \quad & F_{IC}^y = \gamma[1 + \tanh(F_{SOC} - F_{NLL} - \omega F(\Delta f)y')] \\
⑤ \quad & F_{MGB}^x = 1/\{1 + \exp[(F_{IC}^x + F_{IC}^y + nx' - \theta)/k]\} \\
⑥ \quad & F_{MGB}^y = 1/\{1 + \exp[(F_{IC}^x + F_{IC}^y + ny' - \theta)/k]\} \\
⑦ \quad & F_{cortex}^x = I_x F(\Delta f)x' \\
⑧ \quad & F_{cortex}^y = I_y F(\Delta f)y'
\end{aligned} \tag{1}$$

in which the serial numbers and components  $g$ ,  $\beta F(\Delta f)(x' + y')$ ,  $\omega F(\Delta f)x'$ ,  $\omega F(\Delta f)y'$  and  $nx'$ ,  $ny'$  correspond to those in Fig.1(b), and

$$\begin{aligned}
x' &= x - \theta_x \\
y' &= y - \theta_y
\end{aligned} \tag{2}$$

with the firing thresholds  $\theta_x$  and  $\theta_y$ . Since we adiabatically process the neural impulse conduction and the adaptation in the circuit is more complicated at higher hierarchy (62), the adaptation  $\Lambda(x) = a - b \tanh(x' - c)$  and  $\Lambda(y) = a - b \tanh(y' - c)$  are integrated into the final processing of auditory stream. Besides, the inhibitory regulation  $\rho x'$  and  $\rho y'$  with strength coefficient  $\rho$  on the excitation, and the exogenous stimulation  $\sigma$  that may raise from deformation (63) or electromagnetic stimulation (64), etc., are considered. One can see the Appendix for the values of these coefficients. Finally, the deterministic dynamical equations are presented as follows:

$$\begin{aligned}\frac{dx}{dt} &= F_x = \sigma - \rho x' + \Lambda(x) F_{MGB}^x - F_{cortex}^y \\ \frac{dy}{dt} &= F_y = \sigma - \rho y' + \Lambda(y) F_{MGB}^y - F_{cortex}^x\end{aligned}\tag{3}$$

By setting the attention coefficient  $I_x = I_y = 0.0285$  and increasing  $\Delta f$  from 0 to 1, the global auditory dynamical evolution process is traversed (Fig.2(a-f)). Throughout this process, the initially integrated perceptual state fused by strong bilateral excitations gradually diminishes (Fig.2(a, b)). Subsequently, the system encounters the only dynamical bifurcation at  $\Delta f \in (0.4218, 0.4219)$ , being split apart by three saddles into two integrated perceptual states  $Int\ x$ ,  $Int\ y$  that represent the fusion of signals with different frequencies, and two segregated perceptual states  $Seg\ x$ ,  $Seg\ y$  that respectively represent the exclusive excitation of one frequency (Fig.2(c)). At this bifurcation (Fig.2(c)),  $Int\ x$  and  $Int\ y$  are so close that they almost form a single state, despite a saddle not being explicitly depicted between them. As  $\Delta f$  further increases, the polarity of  $Seg\ x$ ,  $Seg\ y$  intensifies, meanwhile  $Int\ x$ ,  $Int\ y$  drift apart from each other.

The dynamics described above naturally reflects the auditory stream segregation process.  $Seg\ x$  and  $Seg\ y$  indicate the segregated perceptions as simultaneous individual auditory streams A\_A\_A\_ and B\_\_B\_\_, while  $Int\ x$  and  $Int\ y$  indicate the integrated stream ABA\_ABA\_. The reason why each state of segregation or integration comprises two states is that one of the A tones or B tones stands in foreground and another is in the background, although it is negligible for the integrated perceptions  $Int\ x$ ,  $Int\ y$  (18, 65).

Beyond the deterministic dynamics, Fig.2(g-n) show the potential landscapes  $U$  and the flux  $\mathbf{J}_{ss}$ , which unveil the essential nonequilibrium dynamical and thermodynamical properties of the system (Eq.(9, 10)). The interactions among the auditory neural circuit, as described by the deterministic neural dynamics  $\mathbf{F}$  and the inherent noise, eventuate the specific distribution of the probability in the phase plane of our system, forming the landscape. The states with higher probability or low potential are reflected on the landscape as basins. These basins correspond to the deterministic attractors and signify the states that carry biological functions (Fig.2(a-f, g-n)). The barriers connecting the basins are formed by the landscape gradient  $-\nabla U$ , which virtually reflect the resistance formed by  $\mathbf{F}$  that points to the attractors. In term of the dynamics, states must overcome this resistance to switch to other basins, which is driven by noise. The high or small noise, characterized by diffusion coefficient  $D$ , will result in low or high barriers, and flat or rough landscapes respectively (Fig.2(j-m)). Therefore, the barrier height can naturally measure the global stability of the states, and correlates to the durations of the auditory perceptions.

However, in a nonequilibrium system, there is the flux  $\mathbf{J}_{ss}$  as the difference between  $-\nabla U$  and  $\mathbf{F}$ . Unlike the landscape gradient force  $-\nabla U$  that drives the states to the bottom of a basin,  $\mathbf{J}_{ss}$  rotationally departs from an attractor, tending to another one in cases of multistability, and even forming circular flows. This introduces the instability of the current state and induces the possibility of new states emerging. When external control conditions change,  $\mathbf{J}_{ss}$  gives rise to the dynamical origin of instability, bifurcations and nonequilibrium phase transitions.

The nonequilibrium landscape reveals that the evolution of auditory dynamics is essentially a continuous phase transition process (16). In the vicinity of the dynamical bifurcation  $\Delta f = 0.4219$ ,  $Seg\ x$  and  $Seg\ y$  basins emerge and gradually deepen as  $\Delta f$  increases, while at a truncation  $\Delta f = 0.8$ ,  $Int\ x$  and  $Int\ y$  basins lose their attraction as perceptual stable states (Fig.2(g-n, o-v), Fig.3(a)). Fig.3(b-i) portray the evolution of the landscape more vividly. Thus, the deterministic dynamics cannot precisely reflect this nonequilibrium phase transition process. In practice, two phase transition points are selected as  $\Delta f = 0.4219$  and  $\Delta f = 0.8$ . On the other hand, the biological system is sensitive to noise, which can only implement its biological function in the effective fluctuation  $D$  range (66), as shown in Fig.3(a). Considering the universality, we take the median of the  $D$  range for each  $\Delta f$  value as the optimal condition.

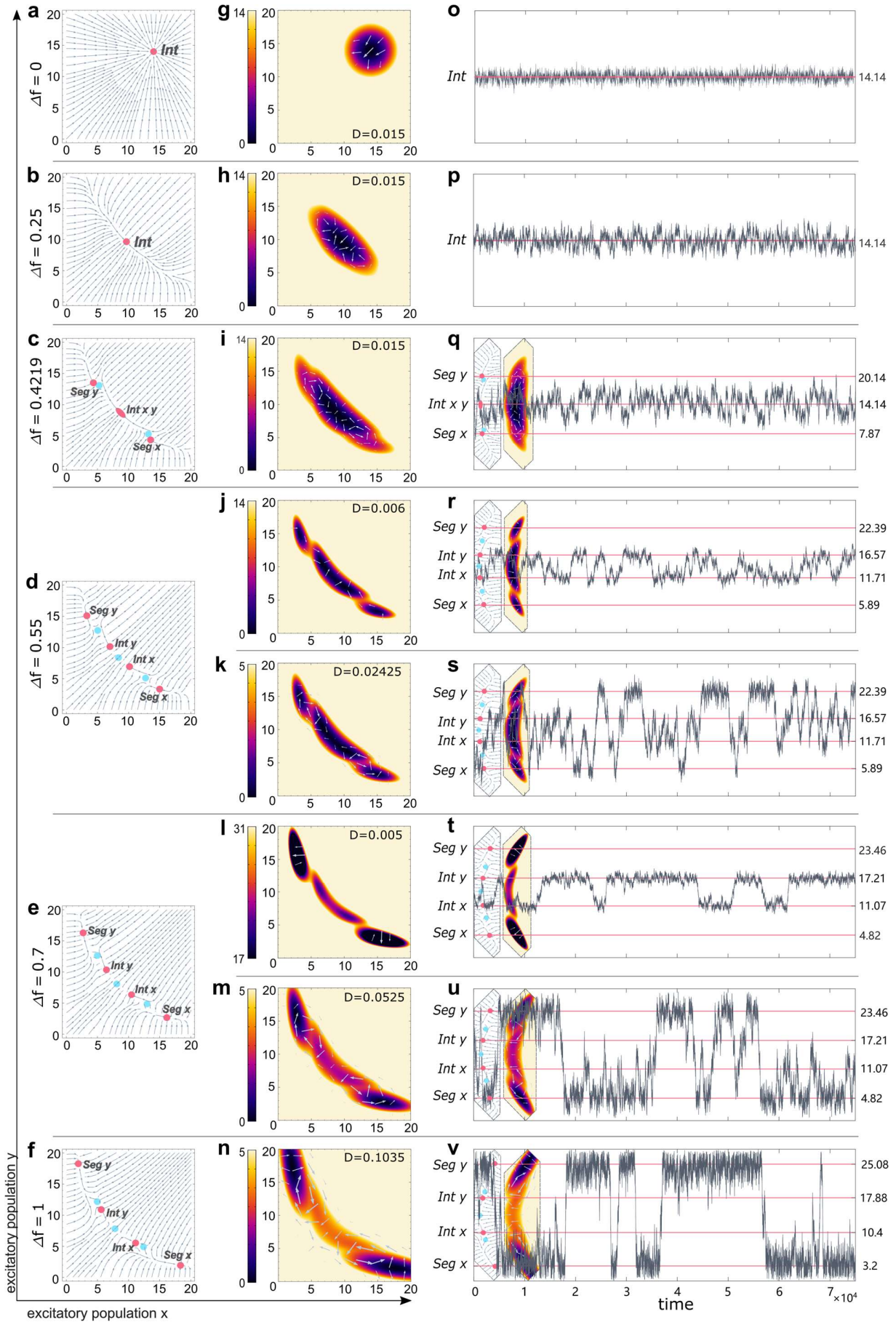


**FIG.2.** Deterministic dynamical structures, landscapes and one-dimensional stochastic series. Attention coefficient  $I_x = I_y = 0.0285$ . Each row of subfigures has a same set of  $\Delta f$  and  $D$ , while **d**, **e** correspond to two  $D$  conditions respectively. **a-f**: Deterministic dynamical structures. Streamlines in these subfigures reveal the global dynamics and the fixed points, in which red solid circles represent the stable states and cyan solid circles represent the saddles. (Int: Integrated auditory perception. Seg: Segregated auditory perception.) **g-n**: Vertical views of landscapes. For an explicit display, the color range of each subfigure is specific. Gray arrows depict the probability fluxes  $\mathbf{J}_{ss}$ , which are taken the logarithm of the real  $\mathbf{J}_{ss}$  values. They reflect the orientation of  $\mathbf{J}_{ss}$ , and where there are significant probability flows. **o-v**: One-dimensional stochastic series. Their scales of the horizontal axes are identical. For each set of  $\Delta f$  and  $D$ , a stochastic trajectory is run in the zone  $x, y \in [0, 20]$ , which the time interval is 0.01 and the total time steps are 75000 (Eq.(7)). Next, each step of the trajectory is vertically projected towards a diagonal line starting from (20, 0) and ending at (0, 20). The positions of the projections are recorded, then they are plotted along the time series to obtain these subgraphs. Each trajectory starts at (10, 10). Slices along the diagonal of deterministic dynamics images and landscapes are proportionally placed in subgraphs (**q-v**) for comparative observation.

Combining the evolution of the deterministic dynamics, the stochastic dynamics (Fig.2(**o-v**)) and the landscapes, the system emanates three practical phases, which are (Fig.1(**c**)):

*Integration* phase, in the range  $\Delta f \in [0.4219, 0.7]$ , is denoted in Fig.3(**a**) as “only Int”. In this case, only the integrated perception *Int* ( $\Delta f \leq 0.4218$ ) or *Int x, y* ( $\Delta f \geq 0.4219$ ) performs the function (Fig.2(**o-q, r, t**)). It manifests that only integrated stream ABA\_ABA\_ can be perceived by human or animal subjects. Along with  $\Delta f$  increasing, the basin on the landscape expands along the diagonal direction, and  $\mathbf{J}_{ss}$  also forms the vortex to the areas where perception  $x$  or  $y$  being solely excited (Fig.2(**h, i**)). This foreshadows the gradual formation of the segregated streams before the emergence of real perception of “auditory bistability” (Fig.2(**o-q**)).

The optimal  $D$  value divides into two branches at  $\Delta f = 0.4219$ . For the range  $\Delta f \in [0.4219, 0.7]$ , the *Integration* phase coincides with the *Rivalry* phase of the “auditory bistability” (Fig.3(**a**)). It is because that when  $D$  value is small, for the integrated perception, two barriers between *Int x, Seg x* and between *Int y, Seg y* are high enough to constrain the states dwelling in the *Int x, Int y* basins for a considerable amount of time (Fig.3(**e, f**)). As evidence, instead of that  $\mathbf{J}_{ss}$  distributes within the areas of the barriers, almost all the  $\mathbf{J}_{ss}$  accumulates in the *Int x, y* basins (Fig.2(**j**)), and gradually transfers to the *Seg x, Seg y* basins (Fig.2(**l**)), manifesting that almost no switching occurs between the integration and the segregation basins. This behavior in  $\Delta f \in [0.4219, 0.7]$  is largely our prediction, based on the fact that during the establishment of the auditory streams, the first perception is always the integrated one, even if  $\Delta f$  is large, and our stochastic simulation complies with that (Fig.2(**r, t**)) (9, 15, 67). Under this condition, a clear distinction between *Int x* and *Int y* implies that the foreground and background of the integrated perception ABA\_ABA\_ can be distinguished (Fig.3(**r, t**)).

Furthermore, a slit exists between the regions of the *Integration* phase and the *Rivalry* phase in the range  $\Delta f \in [0.5, 0.7]$  (Fig.3(**a**)). This is because that the values of  $\Delta f$  and  $D$  locating in this slit lead to the insufficient heights of the barriers between *Int x, Int y* and *Seg x, Seg y*, due to which the states cannot dwell in the *Int x* and *Int y* basins for a long time, and the enormously deep basins of *Seg x, Seg y* will trap the states as a foreground stream almost permanently. This has no practical biological significance so far.

*Rivalry* phase of  $\Delta f \in [0.4219, 0.8]$ , denoted as “Int+Seg” in Fig.3(**a**), depicts the well-known “auditory bistability” observed in the “ambiguity region” of  $\Delta f$  (13, 16, 17, 68). The distinction between the foreground and the background perceptions results in that the segregated stream presents as two states *Seg x, Seg y*. On the other hand, the integrated stream, represented by *Int x* and *Int y*, becomes closely spaced and separated by a shallow barrier, effectively functioning as a single state *Int*. In essence, the global system appears as dynamical tristability with three basins (Fig.2(**k, m**)). Meanwhile,  $\mathbf{J}_{ss}$  forms the prominent vortices traversing the barriers between the basin of *Int* and *Seg x, Seg y*, indicating a high propensity for switching between the integrated streams and two segregated streams (Fig.2(**k, m, s, u**)). As  $\Delta f$  increases, the weights of the *Seg x* basin

representing the segregated streams  $A\_A\_A\_$  and  $Seg\ y$  basin representing  $B\_B\_$  gradually magnify, while those of  $Int\ x$  and  $Int\ y$  progressively diminish. However, even within the transition region  $\Delta f \in [0.65, 0.8]$ , the basins of the integrated stream retain certain residual attractivity for achieving the biological function.

*Segregation* phase of  $\Delta f \in [0.8, 1]$  is denoted in Fig.3(a) as “Seg”. In this phase, although  $Int\ x, Int\ y$  attractors persist, their basin areas perform as a thick barrier, scarcely capturing the states (Fig.2(f, n, v), Fig.3(i)). This manifests the dominance of  $Seg\ x$  and  $Seg\ y$ , corresponding to that the subjects almost exclusively experience alternating segregated streams ( $A\_A\_A\_$  and  $B\_B\_$ ) throughout the psychoacoustic experiment. Despite the integrated perception at the beginning of the build up of the auditory streams, the initial integrated perception maintains transiently (Fig.2(v)) (13, 16, 69). Two  $J_{ss}$  vortices formed on the barriers between  $Int\ x$  and  $Seg\ x, Int\ y$  and  $Seg\ y$  are contiguous to each other, indicating the frequent switching between the two segregated streams. Notably, the persistence of  $Int\ x, Int\ y$  at large  $\Delta f$  as the underlying integrated state should not be disregarded, as supported by the experiment (70, 71).

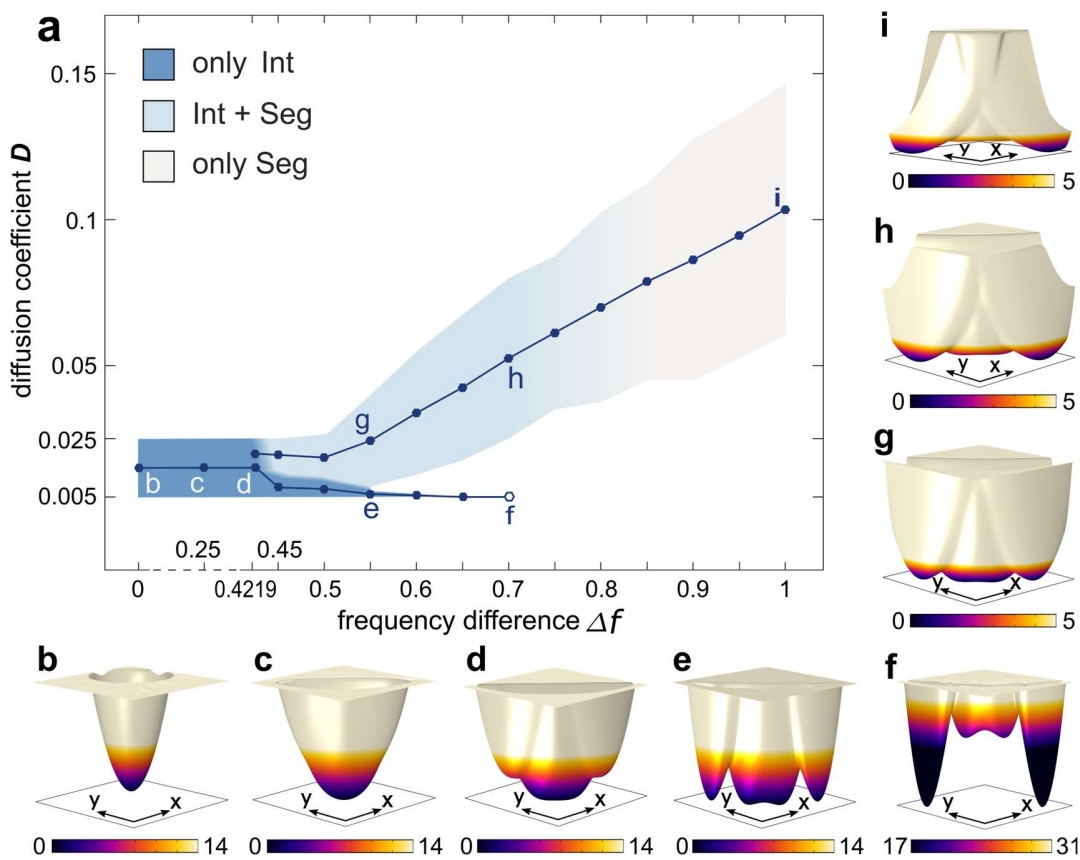


**FIG.3. a:** Effective  $D$  range.  $Int + Seg$  represents the  $\Delta f$  range that integrated and segregated streams exist simultaneously, being the auditory bistability (dynamical tristability). The gradient color range  $\Delta f \in [0.65, 0.8]$  is the transition region from the auditory bistability to the auditory monostability (dynamical bistability) of segregated streams only. The polygonal line in each colored area is the line connecting the medians. **b-i:** The 3D view of landscapes. They correspond to Fig.2(g-n) with the same color range one by one. Their positions in the effective  $D$  range are marked in **a**.

### Dominant kinetic path of the auditory streams switching on the landscape

Beyond the integration phase, both the *Rivalry* and *Segregation* phases exhibit auditory stream switching, contributing to their respective biological functions within a nonequilibrium framework. This stochastic process can be effectively extracted and analyzed through the dominant kinetic path (Eq.(11, 12)), visualized in Fig.4.

The irreversibility inherent to nonequilibrium systems is apparent in the dominant paths. As Fig.4 reveals, these paths and their reverses (mirror symmetry of diagonal line from (0,0) to (20,20), not shown) do not coincide



or pass through the stable attractors or saddles following the landscape gradient. Particularly, by comparing the positional relationship between the path and the fixed point, it is noticed that the dominant paths connecting the two segregated perceptions (Fig.4(a1, b1)) diverge from the combination of the paths connecting  $Seg\ y$  with the integrated perceptions and the paths connecting the integration with  $Seg\ x$  (Fig.4(a2, b2)). This deviation signifies the interplay between the landscape gradient  $-\nabla U$  and flux  $J_{ss}$ .  $J_{ss}$  that induces the nonequilibrium implies the system dissipation. This important property will be explored later.

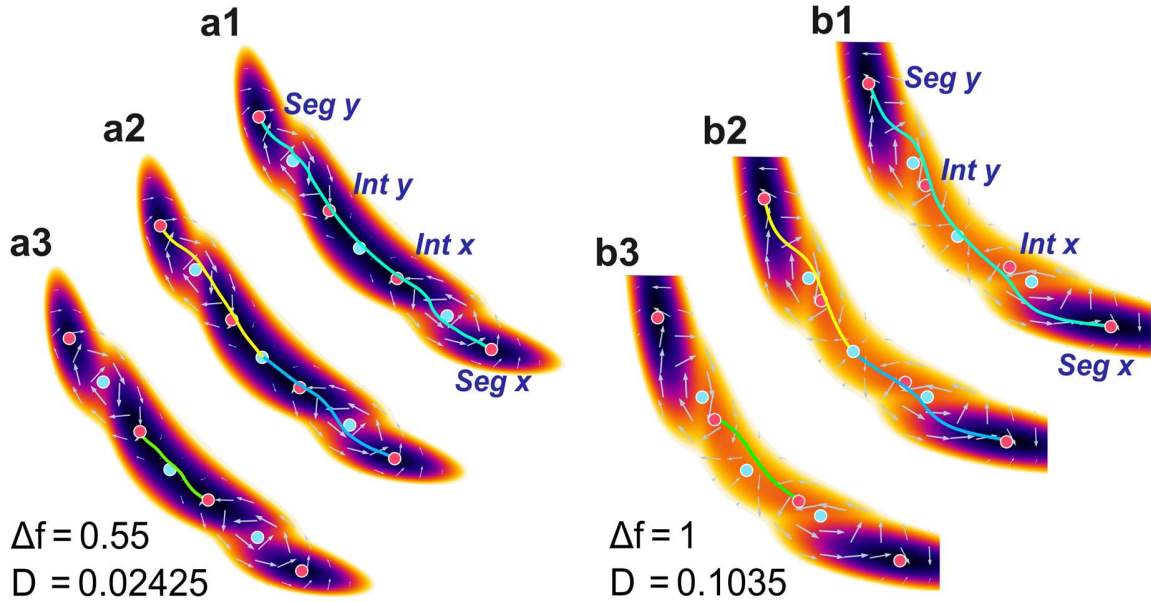


**FIG.4. a1-a3:** Dominant paths of the auditory bistability (dynamical tristability), *Rivalry* phase. **b1-b3:** Dominant paths of the pure segregated streams, *Segregation* phase. For the convenient presentation, **a1-a3, b1-b3** are the landscape basin parts cropped from Fig.2(k, n) respectively, and only the paths along the direction from left top to the right bottom (One of the opposite direction can be simply derived by symmetry). The magenta and baby blue solid circles represent the deterministic stable states and saddles respectively. In **a1** and **b1**, cyan solid lines are dominant paths from  $Seg\ y$  to  $Seg\ x$ . In **a2** and **b2**, yellow lines are paths from  $Seg\ y$  to the middle saddle between  $Int\ x$  and  $Int\ y$ , while blue lines are paths from the middle saddle to  $Seg\ x$ . In **a3** and **b3**, green lines are paths from  $Int\ y$  to  $Int\ x$ . Note that as a rational approach, the middle saddle is accounted start and finish of the paths for the integrated states, according to the fact that  $Int\ x, Int\ y$  perform as one state this case.

The principal contribution of the dominant path analysis predicts that the paths connecting  $Seg\ x$  and  $Seg\ y$  pass through the  $Int\ x, Int\ y$  basins (Fig.4(a1, b1)). It suggests an indirect, intermediated switching process between foreground and background perceptions (A\_A\_ and B\_B\_) though the integrated perception (ABA\_). Due to that the dominant path with its neighborhood possesses the inherently highest probability among all paths linking  $Seg\ x$  and  $Seg\ y$ , this is particularly significant for the *Segregation* phase (Fig.4(b1)). Perceptions of completely segregated auditory streams are also intermediated by integrated streams, although a straight path connecting  $Seg\ x$  and  $Seg\ y$  saves more distance. Experiment I, expounded at the end of results section, confirms this prediction by demonstrating the intermediated nature of foreground-background switching through the integrated perception (Fig.8(c, d)). Especially, the transient ABA\_ perception occurs at large  $\Delta f$  condition of *Segregation* phase, despite the relatively small occurrence number.

The mirror symmetry of the dominant paths and  $Seg\ x, Seg\ y$  basins indicate equal probabilities for both segregated states. Consequently, transition probabilities from the integrated perception to the two segregated perceptions are also even. This suggests that neither A\_ tone nor B\_ tone holds a significant special status. However, reported research on auditory dynamical tristability suggests a potential bias towards segregated stream of the higher tone (72). This nuance highlights the complexity of the issue, which we will revisit later via discussion of the attention effect.

## Duration time and barrier height of the auditory perception

Temporal dynamics, characterized by the duration time of the perceptual states, is a crucial and readily obtainable property in the experiments (16, 17). This behavior arises from the interplay of deterministic forces and noise driving the states on the phase plane, reflected by the nonequilibrium landscape  $U$  and flux  $\mathbf{J}_{ss}$ . We previously explored how landscape barriers influence state kinetics. Here, we delve deeper into the relationship between barrier height (BH) and the durations of auditory perceptions.

For each phase, we define the mean duration time (MDT) as the average of 10000 times that a state starting from a stable point or saddle spends to reach a specific boundary B1, B2 or B3 (Fig.5(a)). For the *Integration* phase, it is the time to reach the boundary B2 from *Int x* or *Int y* attractors. For the *Rivalry* and *Segregation* phases, it is the time for a segregated perception that a state from *Seg x* or *Seg y* attractors reaches the boundary B3 or B1, and the time for the integrated perception that a state from the saddle between *Int x* and *Int y* reaches the boundary B1 or B3. These definitions based on the dynamical switching sequence are previously validated by the results of the dominant path. Correspondingly, a BH is defined as the difference in landscape height between the starting attractor or saddle and the saddle on the boundary crossed during the MDT measurement.

Our model replicates the experimentally observed positive correlation between MDT and  $\Delta f$  for segregated perceptions and the negative correlation for the integrated perception (Fig.5(d)) (13, 14). The underlying mechanism is unveiled by the BH, as higher barriers lead to longer MDTs due to increased stability (Fig.5(b)). Meanwhile, the very low BHs between *Int x* and *Int y* justify treating them as one basin. In Fig.5(b, d), although the BHs of *Int to Seg* at small  $\Delta f$  and *Seg to Int* at large  $\Delta f$  are similar, their corresponding MDTs differ significantly. This can be attributed to the relatively long relaxation time within the wide *Int* basin and the residual attraction of *Int x* and *Int y*. This trend of the MDTs is reflected experimentally when the presentation rate of ABA\_ sequences is relatively small (14). Further, the relaxation also illuminates why the BHs of two sides are almost equal at  $\Delta f=0.55$  but the MDTs meet at  $\Delta f=0.6$ , that is, the shallower *Int* basin at  $\Delta f=0.6$  offsets the relaxation. In fact, Fig.5(d) (part of  $\Delta f>0.55$ ) accurately reproduces experimental measurements of durations in the ‘‘Ambiguous’’ region, with  $\Delta f=0.6$  corresponding to about five semitones (ST) of  $\Delta f$  (13), while Fig.5(d) is precisely consistent with the empirical and modelling results (14).

For the *Integration* phase, two intriguing characteristics emerge. First, the *Int to Seg* BHs decrease from about 9 to 7 as  $\Delta f$  rises, while the *Seg to Int* BHs climb to roughly 27 (Fig.5(c)). This indicates that the *Int* basin retains strong attraction until  $\Delta f=0.7$ , while the segregated basins deepen, making escape from *Seg x* or *Seg y* increasingly difficult. Both factors contribute to the slender tail of the *Integration* phase in the coefficient range (Fig.3(a)). Second, MDTs in Fig.5(c) remain higher than those of *Seg to Int* in Fig.5(d) despite nearly equal BHs in Fig.5(b). This suggests that the MDT still involves the influence of *Seg x* or *Seg y* basins. Based on prior studies employing small presentation rates, our dynamical mechanism for the *Integration* phase at high  $\Delta f$  remains viable (17, 68). Furthermore, the rapid increase in *Int x* and *Int y* MDTs with increasing  $\Delta f$  manifests the gradual emergence of distinct foreground and background perceptions within the integrated stream.

A distinct correlation exists between the BHs and MDTs. Our definition of both stems from the concept of mean first passage time, which, as a first-order approximation, exhibits a positive linear relationship with the  $e$  exponential of the ratio between the deterministic potential difference (integral of  $\mathbf{F}$ ) and  $D$  (25). In the effective range of  $D$  and  $\Delta f$  (Fig.3(a)), increasing  $D$  independently reduces that ratio, presenting as flattening the global landscape without deformation. Thus, the linear relationships present when  $\Delta f$  remains constant (Fig.5(g)). However, Fig.5(e, f) show the tendencies resembling power-law, due to curve bending in specific regions of the fitting lines. In Fig.5(e), the bend occurs after the bifurcation  $\Delta f=0.4219$ , and in Fig.5(f), it happens in the transition region  $\Delta f \in [0.65, 0.8]$  (Fig.3(a)). Recalling Fig.2(a-f, g-n), the distance between the stable states *Int x* and *Int y* rapidly expands after  $\Delta f=0.4219$ , whereas in  $\Delta f \in [0.65, 0.8]$ , the *Int* basin shrinks in weight and domain rapidly, with the opposite occurring for the *Seg x* and *Seg y* basins. The former results in the large gradient of the fitting curve at small  $\Delta f$  in Fig.5(e), and the latter results in the curved midsection in Fig.5(f). This influence of landscape structure is already reflected in the previous content.

In the entire scope of the perceptual rivalry including the auditory stream segregation, the gamma and lognormal distribution of the perceptual durations have been studying for years (13, 14, 17, 73-75). Fig.5(h-j) display our results of the distribution, selecting the situation  $\Delta f = 0.55$  as a sample. We find that the lognormal appears to provide a superior fit for the peak of the distribution, while the gamma distribution fits the remaining segments better. However, the notable non-uniformity in the initial stages, where a majority of states swiftly reach the barriers, emphasizes the significance of the heights and locations of the peaks. As a complement, we suggest the inverse Gaussian distribution, commonly employed for first passage time in Brownian motion with drift (76, 77). It offers a superior fit for the location and height of the peak. Also, this choice aligns with the stochastic nature of our dynamical model.

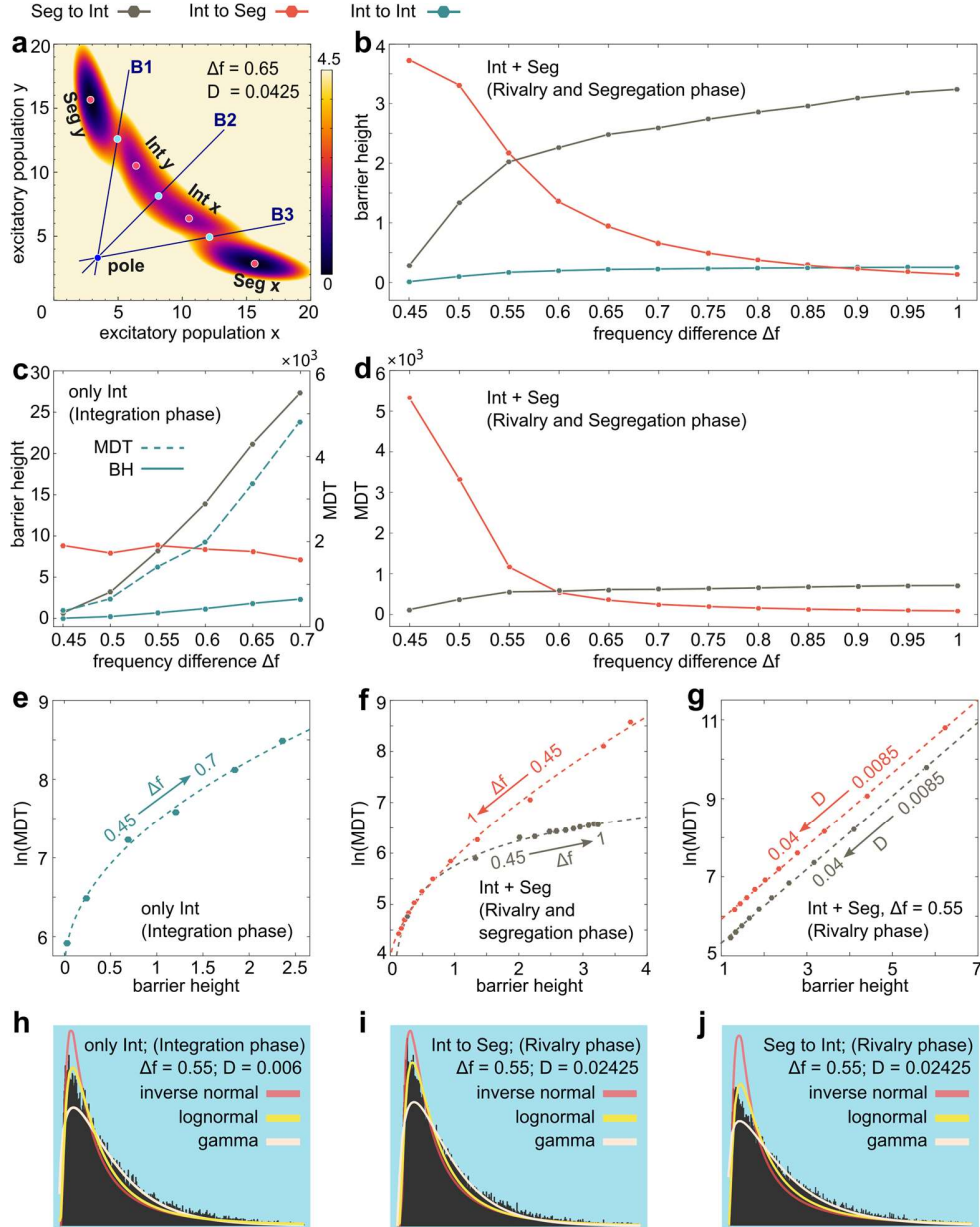


**FIG.5.** **a:** Illustration of the method to measure the duration, for the case  $\Delta f = 0.65$  as an instance. Magenta solid circles represent the deterministic stable states, and cyan ones represent saddles. The three blue lines B1, B2 and B3 are asymptotes of the saddles along the direction of the barriers, which is as the boundaries of the basins. They intersect at the pole. Apparently, the asymptote between  $Int\ x$  and  $Int\ y$  coincides with the diagonal from (0, 0) to (20, 20). **b-d:** Barrier heights and MDT. The  $D$  values of the sampling points are according to the optimal values shown in Fig.3(a). **e-g:** The fittings of the barrier heights and the natural logarithms of the MDT. Fitting method in **e, f** is power law, and linear fitting are employed in **g**. **h-j:** The fitting of the distributions of the durations, selecting case  $\Delta f = 0.55$  as the instance. For explicit display, distribution tails of rare events are cut off.

## Nonequilibrium dynamics and thermodynamics of the auditory stream segregation

As introduced in the section of materials, the nonequilibrium dynamical and thermodynamical properties are manifested through three key quantities: Averaged flux  $\mathbf{J}_{ss}$  (*ave*  $\mathbf{J}_{ss}$ ), entropy production rate (*EPR*) and the difference of the forward and backward cross correlations in time ( $\Delta_{corr}$ ). They respectively represent the stochastic dynamical feature of the flux as the nonequilibrium driving force, the underlying thermodynamics, and the time irreversibility and the degree of the detailed balance breaking of the system. Importantly, these quantities are intricately intertwined, providing a holistic perspective.

Fig.6(a1, a2, b1, b2) reveal a striking parallel between *ave*  $\mathbf{J}_{ss}$  and *EPR*. This mirroring reflects the inherent connection between their equations (Eq.(13, 14)). Within the effective  $D$  range, as  $\Delta f$  increases, *ave*  $\mathbf{J}_{ss}$  remains very low during the *Integration* phase before the bifurcation  $\Delta f \simeq 0.4219$ , then sharply rises at the onset of the *Rivalry* phase and plateaus throughout the transition region  $\Delta f \in [0.65, 0.8]$ . Finally, in the *Segregation* phase, a slight decline is observed (Fig.6(b2, b3, b4)). This behavior can be understood considering the role of  $\mathbf{J}_{ss}$  in tearing the attractors apart and forming stable cycle flows between them. Evidently, the *Rivalry* phase with three basins facilitates such flows, demanding more  $\mathbf{J}_{ss}$  flux for supporting its global dynamical structure. In contrast, the *Segregation* phase features a shallow *Int* basin for connecting the *Seg x* and *Seg y* basins, leading to the observed decline. Furthermore, in the *Integration* phase, the single attractor necessitates minimal *ave*  $\mathbf{J}_{ss}$  compared to other cases, reflecting its simpler dynamical structure with minimal flow requirements. On the other hand, *EPR* depicts the cost of the energy, work and dissipation. Its difference from *ave*  $\mathbf{J}_{ss}$  is that the cost reflected by *EPR* of the *Segregation* phase remains comparable to the *Rivalry* phase (Fig.6(a2)). This highlights the distinction between dynamics and thermodynamics: although thorough segregation requires less  $\mathbf{J}_{ss}$ , the cost of maintaining the *Segregation* dynamical structure remains significant due to the frequent states switching. This switching primarily relates to crossing the landscape barriers, where  $\mathbf{F}$  and  $\mathbf{J}_{ss}$  present strongly ( $\mathbf{F}$  almost coincides with landscape gradient  $-D\nabla U$ ). Considering that  $\int_{\Omega} \mathbf{F} \cdot \mathbf{J} d\Omega$  (Eq.(14)), the *Rivalry* phase has two barriers with relatively large gradient, while  $\mathbf{J}_{ss}$  in *Segregation* phase is more intense and distributes more densely. Consequently, two phases exhibit comparable *EPR* levels. This analysis corresponds with the simulation results: more  $\mathbf{J}_{ss}$  manifests more frequent switching, implying that more cost is required to support the dynamical process.

Although the *Integration* phase has the switching between the foreground and background streams of *Int x* and *Int y* with high  $\Delta f$  and small  $D$  as discussed previously, the seemingly contradictory observation of high *ave*  $\mathbf{J}_{ss}$  and low *EPR* can be explained by considering ensemble averages in physics (Fig.6(a2-a4, b2-b4)). From the cases  $\Delta f = 0.55$  (Fig.2(j)) to  $\Delta f = 0.7$  (Fig.2(l)), as  $\mathbf{J}_{ss}$  in the *Int* basin dwindles to zero, it concurrently accumulates in the *Seg x* and *Seg y* basins, bypassing the barriers almost entirely. This explains the high *ave*  $\mathbf{J}_{ss}$ , as it reflects  $\mathbf{J}_{ss}$  distributed in basins of large weights. In this case, except for stochastic switching across the shallow barrier between *Int x* and *Int y*, there are few switches between the integrated and the segregated streams. Neither dwelling in a deep *Seg x*, *Seg y* or *Int* basin nor roaming in large *Int* basin requires significant work or dissipation cost. Therefore, despite perceptual alternation between the foreground and background streams, *EPR* remains low in the *Integration* phase of  $\Delta f \in [0.4219, 0.7)$  as before the bifurcation  $\Delta f \simeq 0.4219$ . In the sense of minimum cost, the auditory neural system achieves the switching between foreground and background by the integrated stream more easily than in *Rivalry* or the *Segregation* phase, although the former is less discovered experimentally.

A special and significant case occurs at  $\Delta f = 0.55$  with three equally weighted basins, where *EPR*, *ave*  $\mathbf{J}_{ss}$  and later-discussed  $\Delta_{corr}$  exhibit remarkable peak, extending beyond the effective  $D$  range (Fig.6(a2-a4, b2-b4, c2-c4)). In this case, at the optimal  $D$  values ( $D = 0.006$  for *Integration* phase and  $D = 0.02425$  for *Rivalry* phase), the interactions between the switching frequency among the basins and the resistance caused by the barriers achieve the optimal dissipation efficiency (Fig.2(r, s), Fig.6(a3, a4)). Necessarily, this efficiency requires substantial cost, particularly for the *Rivalry* phase at  $D = 0.02425$  (Fig.6(a3, a4)). The intensive rotational flux  $\mathbf{J}_{ss}$  plays a key role in this process (Fig.6(b3, b4), Eq.(13)).

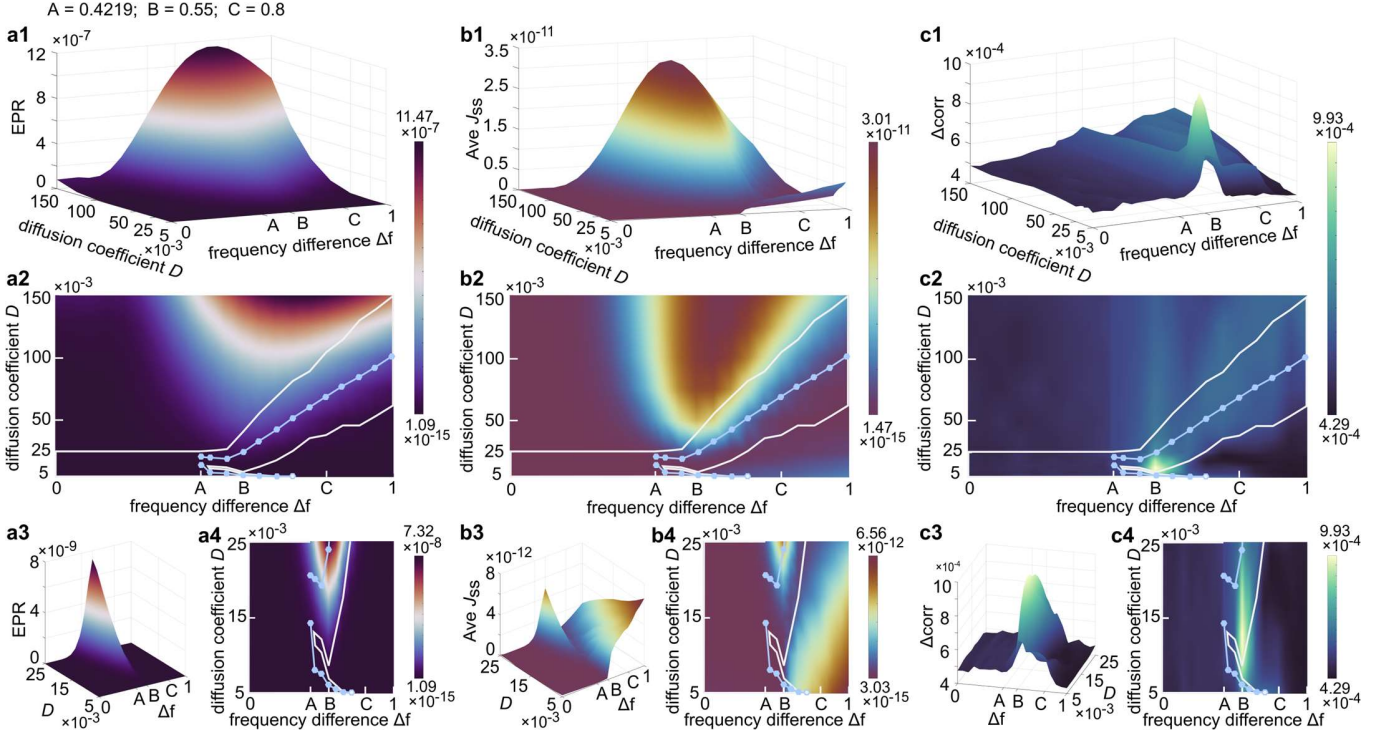


**FIG.6.** Illustrations of  $EPR$ , averaged  $J_{ss}$  and  $\Delta corr$  in the coefficient space of  $\Delta f$  and  $D$ . On the axis of  $\Delta f$ , A and C are bifurcations between *Integration*, *Rivalry* and *Segregation* phases, while B represents the case with three equally weighted basins. Subfigures **a2**, **b2**, and **c2** are the vertical views of the **a1**, **b1**, and **c1**, in which the areas with the white polygonal edges are the practical  $D$  ranges according with Fig.3(a), and the blue points on the blue polygonal lines are the optimal  $D$  values after the bifurcation  $\Delta f \in [0.4218, 0.4219]$ . Subfigures **(a3, a4)**, **(b3, b4)**, and **(c3, c4)** show the situations of small  $D$  values.

Although only one real bifurcation occurs at  $\Delta f \simeq 0.4219$  in the deterministic dynamics, the sharp ascent and descent of  $EPR$  and  $ave J_{ss}$  reflect the phase transitions in terms of the nonequilibrium dynamics and thermodynamics, as unveiled by the landscapes and fluxes. Fig.6(**a2, a4, b2, b4**) shows that along with the optimal  $D$  values, the bifurcation ( $D = 0.02425$ ,  $\Delta f \simeq 0.4219$ ) locates on the steep slope of  $EPR$  and  $ave J_{ss}$ . Furthermore, the optimal  $D$  values consecutively appear on the slopes of both  $ave J_{ss}$  and  $EPR$  from the beginning of the transition region  $\Delta f \in [0.65, 0.8]$  to the end of the *Segregation* phase. This suggests that the entire process, especially the transition region, operates as a continuous phase transition where three basins of *Rivalry* phase gradually emerge and then transform into two effective basins in the *Segregation* phase. In a view of the phase transition, this ongoing transformation naturally requires substantial cost to sustain. In fact, as  $\Delta f$  approaches very high values ( $\Delta f \gg 1$ ), the *Int* basin vanishes, implying that the *Rivalry* and *Segregation* phase are a segment during dynamical monostability (*Integration* phase) evolving into dynamical bistability. *Seg x* and *Seg y* in this dynamical bistability cannot mutually switch due to the excessively high  $\Delta f$ .

Ultimately, phase transitions in our model can be traced back to symmetry breaking in physics. This is captured by  $\Delta corr$ , which measures time irreversibility and detailed balance breaking, reflecting the deviation from equilibrium (Eq.(15)). Significantly, a cliff-like step arises at the bifurcation  $\Delta f \simeq 0.4219$  in the global coefficient space, marking a definite phase transition (Fig.6(**c1-c4**)). Similarly, the continuous ridge observed in the practical  $D$  range suggests a continuous phase transition, resembling those of  $ave J_{ss}$  and  $EPR$ . Compared to the monostability of *Integration* phase, the dynamical structures with multiple attractive basins display a complex dynamical behavior, which leads to a strong breakdown of the detailed balance of the system, namely intensely diverging from equilibrium.

The strong correlation observed between  $ave \mathbf{J}_{ss}$ ,  $EPR$ , and  $\Delta_{corr}$  are not coincidental. The detailed balance breaking is induced by the directional probability flux  $\mathbf{J}_{ss}$  that generates non-uniformity within the system, necessitating significant cost to drive these dynamic processes. The most consistent features across  $\Delta_{corr}$ ,  $EPR$  and  $ave \mathbf{J}_{ss}$  arise at  $\Delta f = 0.55$  around the optimal  $D$  value. Here,  $\Delta_{corr}$  exhibits peak values exceeding any other region, reflecting its unique sensitivity (Fig.6(c1, a3, a4, b3, b4, c3, c4)). Interestingly,  $\Delta_{corr}$  for the *Integration* phase at large  $\Delta f$  values remains a high level until  $\Delta f = 0.7$ , despite the continuously increasing  $ave \mathbf{J}_{ss}$  up to the  $\Delta f$  range of the *Segregation* phase (Fig.6(b2-b4)). As Fig.5(c) shows, when  $D$  is very small and  $\Delta f > 0.7$ , the states become readily trapped in either of the two segregated basins due to the very high barriers, leading to a monostability-like situation without switching between two segregated streams. These findings not only underscore the importance of the equally weighted case ( $\Delta f = 0.55$ ) but also hint that significant  $\Delta_{corr}$  values only emerge within the  $D$  range relevant to biological functions. Excessively strong noise neutralizes the interactions among the neural circuit, leading to a flatten landscape that resembles pure Brownian motion, while too small noise weakens switching between basins, neither of which embodies the detailed balance breaking through the finite auditory perceptual data sequence.

A key advantage of  $\Delta_{corr}$  is its ability to detect the significant theoretical properties,  $EPR$  and  $ave \mathbf{J}_{ss}$ , due to their similar tendencies. Importantly,  $\Delta_{corr}$  can be readily obtained experimentally by calculating the difference between forward and backward time trace cross correlations, requiring only recorded sequences of the neural population signals. These signals have been widely measured in studies via fMRI (54, 57), EEG or ECoG (58, 61, 78, 79), and invasive cerebral electrophysiological measurement for animal subjects (80, 81). Additionally, advancements in tonotopic mapping on the cortex provide the feasibility of tracking the cortical positions of specific frequencies used in our model calculations (54, 61, 82). We will discuss further in the Discussion section.

### Attention as the principal structural parameter

The mechanism of the auditory streams cannot avoid the influence of the attention. Unlike an idealized constant, attention fluctuates around a baseline value ( $I_x = I_y = 0.0285$  in our model), until the listener alters it consciously. This manifests as intended switches between different streams, where the attended stream becomes dominant while others fade. Attention, therefore, acts as an asymmetric regulator of potential dynamics.

Postulating that  $I_x$  and  $I_y$  can be amplified or abated simultaneously, we propose the fundamental principle of attention-modulated dynamics:

*Principle:* Given that all the auditory dynamical phases (e.g., Fig.2(a-f, g-n)) uniquely map onto  $\Delta f$  values in the range  $[0, 1]$  with the baseline  $I_x = I_y = 0.0285$ , simultaneously amplifying  $I_x$  and  $I_y$  will shrink the  $\Delta f$  range to  $[0, \kappa < 1]$  and vice versa.

Fig.7(b1-b4, b5-b8) support the *Principle* through simulations. With a fixed  $\Delta f = 0.55$ , the landscapes of Fig.7(b5-b8) resemble those of Fig.3(b, d, h, i) with the same  $D$  values and modified  $I_x = I_y$  values. Fig.7(a) shows the scaled  $\Delta f$  ranges required for the entire phase transition process under varying  $I_x = I_y$  values. Given that  $\Delta f = 0$  in each cell of right column in Fig.7(a) represents the *Integration* phase, it confirms that regardless of attention changing, only the *Int* perception occurs at the limit  $\Delta f = 0$ . This is because that with only one single tone being listened to, attention cannot be divided. It indicates a limit in frequency resolution during the auditory scene analysis, which originates from the structure of the entire auditory neural network rather than cochlear mechanics (43). As attention is indispensable for auditory stream organization (83), another theoretical limit exists at  $I_x = I_y = 0$ , under which the system presents only the *Int* perception with finite  $\Delta f$  (Fig.7(a, b1, b5)). This implies that abating attention leads to the system degenerating to a lower  $\Delta f$  phase with the original  $I_x = I_y$ , resulting in a more dominant *Int* perception and decaying segregated perceptions.

Practically, it is difficult for human listeners to increase the attention on both segregated perceptions independently and simultaneously. However, abating bilateral attention simultaneously is feasible. This allows us to test the *Principle* by regulating attention abatement levels. It can be anticipated that stronger attention abatement will lead to higher dominance of the integrated perception, exceeding those observed with baseline

attention except in the *Integration* phase (83). Experiment II, described in the next subsection, supports this anticipation. Here, distraction time length serves to quantify the auditory attention abatement.

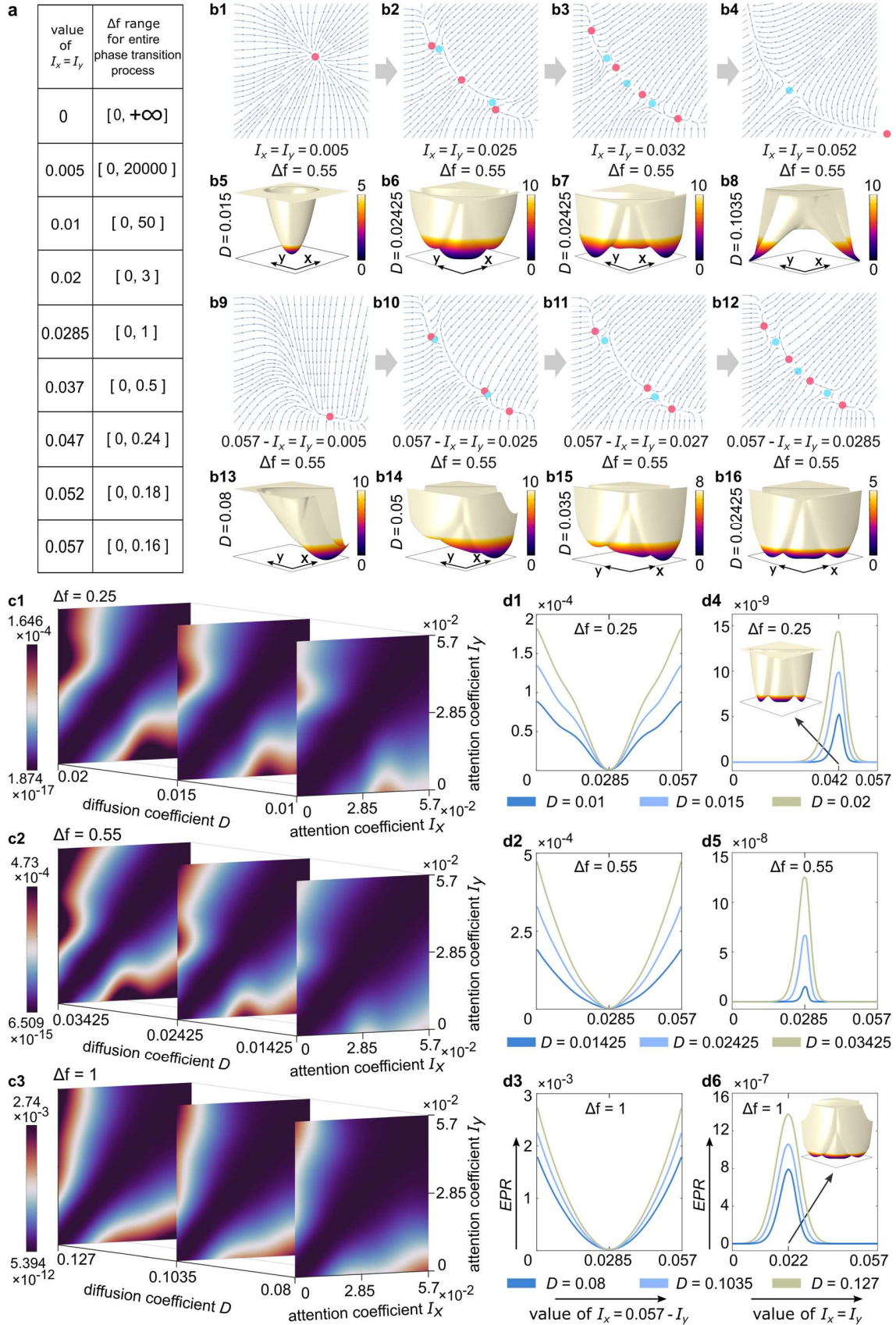


**FIG.7. a:**  $\Delta f$  ranges for completing entire dynamical phase transition process under different values of  $I_x = I_y$ . **b1-b4, b5-b8:** Examples of deterministic dynamical structures of  $\Delta f = 0.55$  with different values of  $I_x = I_y$ , and corresponding landscapes.  $D$  values of these landscapes correspond to points b, d, h, i in Fig.3(a). **b9-b12, b13-b16:** Examples of deterministic dynamical structures of  $\Delta f = 0.55$  with different values of  $I_y = 0.057 - I_x$ , and corresponding landscapes.  $D$  values of these landscapes are selected properly in the practical range in Fig. 3(a). **c1-c3:**  $EPR$  values in range of  $I_x, I_y \in [0, 0.057]$ .  $\Delta f = 0.25, 0.55, 1$  respectively correspond to *Integration, Rivalry* and *Segregation* phases, for each of which three subgraphs of  $D$  values are selected in the practical range in Fig.3(a) and the median values are the most proper  $D$  value. **d1-d3:**  $EPR$  values on diagonal  $I_x + I_y = 0.057$  of three subgraphs, respectively corresponding to **c1-c3**. **d4-d6:**  $EPR$  values on diagonal  $I_x = I_y$  of three subgraphs, respectively corresponding to **c1-c3**. In **d4** and **d6**, there are landscape diagrams corresponding to the situations of peak values, and landscape for the peak value in **d5** is **b16**.

More commonly, listener focuses on a certain perception in the auditory scene, leading to unequal attentions ( $I_x \neq I_y$ ). From the *Principle*, dividing the phase plane diagonally from (0, 0) to (20, 20), each side of the auditory dynamical structure will degenerate or evolve separately based on current  $\Delta f$ . However, increased attention on one side naturally reduces attention on the other (40, 83). Hence, we presume that  $I_x + I_y = 0.057$  under unequal attention conditions. Fig.7(**b13-b16**) demonstrate that as attention increases on one side, the corresponding basin gains higher weight and larger domain, while the opposite occurs on another side. Further, considering that simultaneously abating  $I_x$  and  $I_y$  is equivalent to amplifying a “quasi attention” on the integrated perception, Fig.7(**b1-b8**) reinforce our theory.

When attention on one side is sufficiently high, the basin of another side vanishes, aligning with experimental findings (41, 42). These transitions stem from changes in the underlying deterministic dynamics (Fig.7(**b9-b12**)). Particularly, as attention imbalance increases, the stable state *Int x* or *Int y* on the side with lower attention vanishes first. In fact, during the unfettered preparation stage for Experiment II, most subjects reported short and specious integrated perception when concentrating on a segregated perception, the tones being inaccurate and adhering to each other. This suggests the residual presence of *Int x* or *Int y* (Fig.7(**b10, b11, b14, b15**)). Additionally, major transition happens in a small range of the  $I_x$  and  $I_y$  (akin to the deterministic dynamical structure as Fig.7(**b9**) when  $I_y = 0.057 - I_x < 0.025$ ), highlighting the sensitivity of the modulation by unequal attentions (84).

Fig.7(**c1-c3**) exhibit the global  $EPR$  maps with  $I_x, I_y$  as parameters. The upper and lower limits of the color legends on the left side of each subfigure represent the generally increasing  $EPR$  values of the global maps following the  $\Delta f$  increasing. Meanwhile, in each subfigure,  $EPR$  values of the global maps increase along with  $D$  enlarging. These are in line with the conclusions determined in Fig.6(**a1, a2**) even if under modulation of the attentions. Notably, higher  $EPR$  occurs around larger imbalance between  $I_x$  and  $I_y$  (top-left and bottom-right corners in each subfigure), while minimum  $EPR$  lies along the  $I_x = I_y$  diagonals. This indicates that focusing attention on one side incurs higher cost compared to spontaneously balanced attention. Fig.7(**d1-d3**) entrench this, as minimum  $EPR$  precisely occurs at  $I_x = I_y = 0.0285$ .

The impermanence of attention-driven individual perceptions stems from their high thermodynamical cost and deviation from equilibrium, similar to neural adaptation (62, 85). Nonetheless, balanced attention does not always guarantee minimum  $EPR$ . As discussed earlier, maximum  $EPR$  and detailed balance breaking arise when basins have equal weights, requiring the most cost to sustain intense dynamics (Fig.7(**d4-d6**)). In a sense, the  $\Delta f$  and the  $I_x, I_y$  are complementary to each other. Ultimately, the underlying dynamics of holistic neural pathways, not just attention modulation or  $\Delta f$ , dictate the thermodynamic and energetic behavior.

### Psychoacoustic experiments

Ten healthy-hearing subjects (average age 25.3, with 3 females) participated in two psychoacoustic experiments after providing informed consent for the entire procedure and data usage. Experiments were conducted in a soundproof chamber, and all subjects demonstrably understood the presented auditory signal types. Stimuli were generated using MATLAB and its Psychtoolbox extension. Both experimental data and code are available with this article.0



**Experiment I:** This experiment investigates whether the integrated auditory streams ABA\_ABA\_ (*Int* perception) intermediates the foreground-background switch between segregated streams A\_A\_A\_ (*Seg x* perception) and B\_B\_ (*Seg y* perception). Subjects listened to 20 repetitions of long ABA\_ sequences presented through earphones. Each repetition varied in  $\Delta f$  (4ST, 8ST, 12ST, 16ST, 20ST) and tone duration (100ms, 150ms, 200ms, 250ms, corresponding to 10Hz, 6.667Hz, 5Hz, 4Hz rates). In one sequence, the durations of tone A, tone B and blank are equal. All sequences had equal durations for tones A, B, and silent blank, and included 10ms smooth frequency transitions between tones (Fig. 8(c)). For balance attention, tone A had double the repeating frequency of tone B (Fig.8(a)).

Each trial consisted of 15 subtests. After initial stream organization, if subjects perceived A\_A\_A\_ as the more distinct foreground, they pressed " $\leftarrow$ ". They were then allowed to mildly shift attention to B\_B\_ (foreground-background switch not guaranteed to happen in every time of segregated perception). Subjects pressed " $\downarrow$ " on the keyboard if they perceived the integrated ABA\_ABA\_ sequence, then " $\rightarrow$ " if they identified B\_B\_. Time lengths between " $\downarrow$ " and " $\rightarrow$ " were recorded. If they directly switched to B\_B\_ without integrated perception, they pressed "0" (recorded time was 0). Note that the delay between identifying ABA\_ABA\_ (" $\downarrow$ ") and its actual occurrence was compensated by the next delay that happened when " $\rightarrow$ " was pressed. The procedure was identical when the subtest began with " $\rightarrow$ " for B\_B\_ perception.

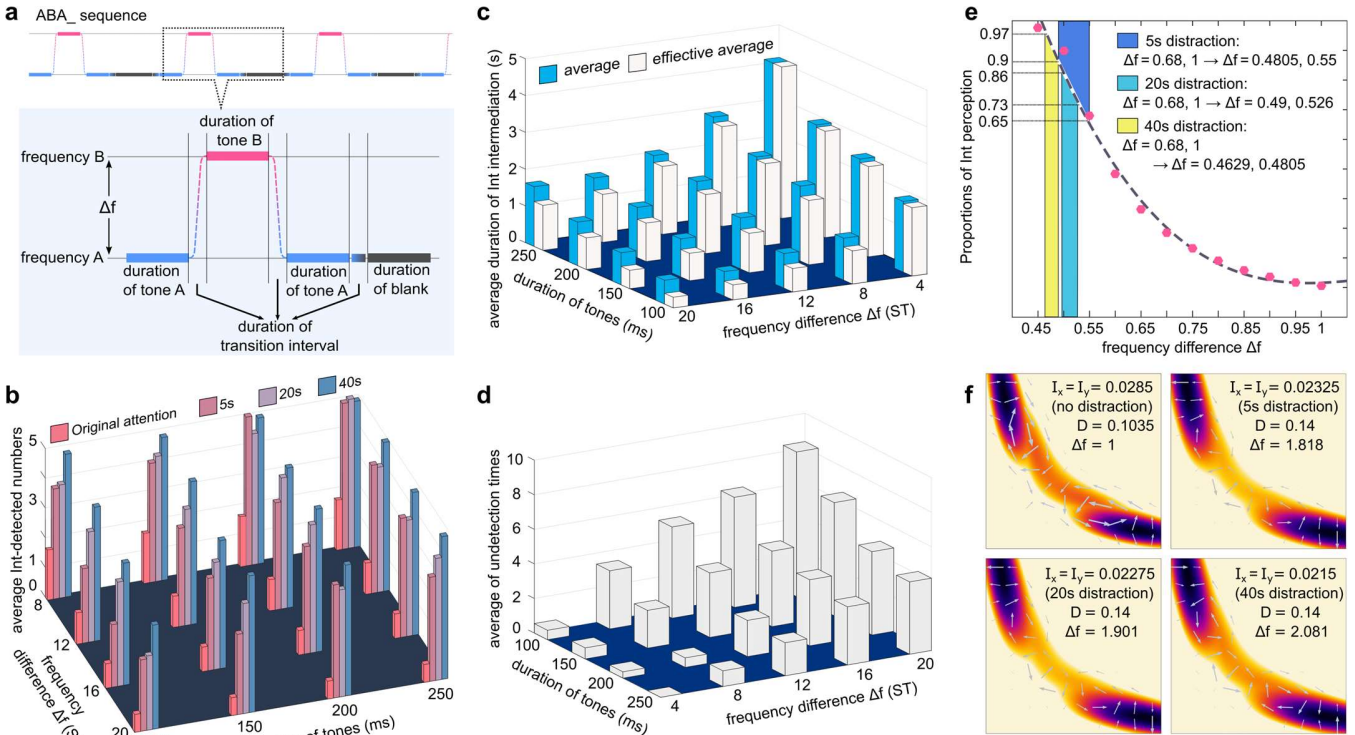


**FIG.8. a:** Illustration of the structure of the ABA\_ auditory sequences. **b:** Average numbers that the subject perceived the integrated perception after 5s, 20s and 40s distractions, and predicted results without distraction (original attention). **c:** Average durations of the integrated perception for intermediation during the foreground-background switching of the segregated perceptions. "average" (blue bars) denote the results processed by Eq.(4), and "effective average" (white bars) denote the results processed by Eq.(5). **d:** Average numbers that the subjects did not detect the intermediating integrated perception, obtained by Eq.(6). **e:** Scaled  $\Delta f$  ranges under 5s, 20s, 40s distractions corresponding to  $\Delta f \in [0.68, 1]$  (8ST, 20ST), according to the proportions of *Int* perception calculated by the original model (Fig.5(b)). Magenta points are *Int*-perception proportions under different  $\Delta f$  values, with a dash fitting line. **f:** Ends of the phase transition process under 5s, 20s, 40s distractions, corresponding to  $\Delta f = 1$  in original model.

Setting that for a certain couple of parameters, a data from the  $i$ -th subject ( $i=1, 2, \dots, 10$ ) in the  $j$ -th subtest ( $j=1, 2, \dots, 15$ ) is  $X_i^j$ , and the total number of the data being zero is  $M_i$ , the average duration of the intermediating *Int* perceptions is defined as:

$$\frac{1}{10} \sum_i \frac{\sum_j X_i^j}{(15 - M_i)} \quad (4)$$

and the effective average duration reads:

$$\frac{1}{10} \sum_i \frac{\sum_j X_i^j}{15} \quad (5)$$

The average number that the subjects did not detect the intermediating integrated perception is:

$$\frac{1}{10} \sum_i M_i \quad (6)$$

Fig.8(c, d) present the average durations of intermediary *Int* perceptions and the number of subjects who did not detect intermediary *Int* perceptions. Consistent with our model, large  $\Delta f$  (16ST, 20ST) resulted in short durations (Fig. 8(a1)) and infrequent *Int* detection. This aligns with the landscape, where the *Int* basin resembles a wide barrier between *Seg x* and *Seg y* basins rather than an attractive basin (Fig.2(n), Fig.3(i)). As  $\Delta f$  decreases, the landscape transforms from *Segregation* to *Rivalry* and *Integration* phases, where the ability of *Int* basin to trap the states increases (Fig.2(i, k), Fig.3(d, g)). For  $\Delta f < 5ST$ , *Int* perception is no longer considered an intermediary state. Viewing intermediating *Int* as an independent stream, Fig.8(c) aligns with experiment (14), suggesting longer tones provide more time to identify the end of *Int* perceptions. However, Fig.8(d) indicates that tone duration also affects the dynamics, with shorter durations attenuating the attraction of *Int* basin. See the Discussion section for further details.

**Experiment II:** This experiment aims to validate the *Principle* that attention diversion weakens the dynamical structure of high  $\Delta f$ , as decreasing  $\Delta f$  itself. The number of detected *Int* perceptions after distraction served as the indicator. Auditory stimuli were identical to Experiment I (excluding  $\Delta f = 4ST$  that *Int* perception dominates).

In a test of each set of tone duration and  $\Delta f$ , the fifteen subtests consist of randomly sorted distraction time lengths 5s, 20s and 40s for five times each, aiming to quantify the degrees of distraction. After establishing stable segregated streams (*Seg x*, *Seg y* perceptions), subjects were instructed to press any key on the keyboard. They were then requested to immediately divert attention (e.g., check the mobile phone silently). A transient warning signaled the end of the distraction period, prompting subjects to return attention to the auditory stimuli. *Int* perception was indicated by pressing "spacebar," otherwise any other key was pressed.

Two key points require consideration. First, pinpointing the precise dynamical phase that the system degenerates into under different distraction levels is challenging. Even assuming the *Rivalry* phase, detecting *Int* perception remains probabilistic. This inherent variability is addressed statistically: averaging results across multiple subjects allow us to approximate the true expected value within the altered dynamical structure. Second, we need to confirm whether degeneration occurs at all. Leveraging MDT results (Fig. 5(d)), we treated 5ST and 20ST as proxies for  $\Delta f = 0.6, 1$ , respectively (8ST corresponds to  $\Delta f = 0.68$ ). We then calculated the proportions of detected *Int* perceptions for 8ST, 12ST, 16ST, and 20ST across five-times tests ("Original attention" bars in Fig. 8(b)). These proportions were significantly lower than any observed ones under any  $\Delta f$ , tone duration, or distraction length condition (Fig.8(b)). This aligns with similar conclusions drawn from empirical results in Ref. (14). Further, longer distraction apparently results in a higher probability of *Int* perception. Along with  $\Delta f$  decreasing, trends of the results reveals that 5s distraction (average *Int* detections 2-5) degrades the dynamical structure into the *Rivalry* phase, while 40s distraction (numbers reaching 5) leads the dynamical structure to be very close to the *Integration* phase. These results shown in Fig.8(b) confirm that the weakened attention eventuates the enhancement of the *Int* basin on the landscape when  $\Delta f$  remains constant, being

equivalent to a degeneration of the dynamical structure. In other words, the  $\Delta f$  range for entire auditory phase transition process is elongated, as predicted by the *Principle* mentioned in the previous section.

Provided that the average data of 150ms and 200ms correspond to the optimal conditions of our model (Fig.3(a)), the proportions of *Int*-detected numbers among the five-times tests, corresponding to 8ST and 20ST ( $\Delta f = 0.68, 1$ ) respectively, are: (0.65, 0.9) for 5s distraction, (0.73, 0.86) for 20s distraction, and (0.9, 0.97) for 40s distraction. Fig.8(e) shows the  $\Delta f$  ranges corresponding to these pairs of *Int* proportions when attention is at the baseline ( $I_x = I_y = 0.0285$ ). Thus, the ends of scaled  $\Delta f$  ranges for entire phase transition process under 5s, 20s and 40s distraction are  $1/0.55 \approx 1.818$ ,  $1/0.526 \approx 1.901$  and  $1/0.4805 \approx 2.081$ , corresponding to  $\Delta f = 1$  (20ST) in the original model. The parallel  $I_x$  and  $I_y$  values can be determined by the landscapes (Fig.8(f)). At these scaling,  $\Delta f = 0.68$  (8ST) in original model corresponds to  $0.68 \times 0.55 = 0.374$  (5s distraction),  $0.68 \times 0.526 \approx 0.3577$  (20s distraction), and  $0.68 \times 0.4805 \approx 0.3267$  (40s distraction), which sink into the *Integration* phase. However, they are different to the experimental results in Fig.8(e) that are beyond the bifurcation  $\Delta f = 0.4219$ . Even under 40s distraction with high  $\Delta f$  (16ST, 20ST), segregated streams still occurred, aligning with previous research (65, 83). In fact, our framework allows for this slight deviation. As shown in Fig.2(h, i), states have the potential to lean towards the segregated perceptions, even without deterministic attractors *Seg x* or *Seg y*. Experimental reports also demonstrate that the absolute integrated perception can only arise when  $\Delta f$  is very small (13). These results confirm the continuous nonequilibrium phase transition process of the auditory stream segregation, where the deterministic bifurcation cannot predict the occurrence of phase transition independently. It originates from the holistic structure of the auditory neural pathways.

## Discussion

**Intermediation by the integrated perception.** Existing research, without discriminating the foreground or the background, has reported the fast switching intermediated by the integrated perception (13, 17, 41, 86). Reference (72) elucidates auditory tristability using "energy landscapes" and hints at switching intermediated by integrated perception. Besides, the Markovian property of our system and dominant path analysis suggest that the switching between *Seg y* to *Seg x* can be viewed as two independent processes: *Seg y* to *Int* followed by a probabilistic switch within *Int* to *Seg x* (Fig.4(a1, a2, b1, b2)). This aligns with the hierarchical competition framework of predictive coding (15), where the system returns to competition among sound event organizations, temporarily selecting the integrated organization before probabilistically selecting the segregated organization and transitioning to the  $B_-$  event. These explanations are mutually compatible. Further, this rivalry between different auditory perceptions, in which an *Int* state intermediates, seems to be a simple brain decision making process, due to that they present the similar dynamical behaviors (87). This similarity is particularly significant when it comes to attention regulation, corresponding to "change of mind" in decision making.

**Thermodynamics and Neurophysiology.** Despite growing theoretical interest in cerebral and auditory energetics (29-31, 88, 89), quantifying energy costs in large neural populations remains challenging for traditional methods. quantifying energy costs in large neural populations remains challenging with traditional methods. Our nonequilibrium dynamics and thermodynamics approach offers a potential solution. Non-intrusive, semi-invasive or invasive test can collect data for  $\Delta_{corr}$  calculation without harming biological activity (54, 57, 58, 61, 78-81). Notably,  $\Delta_{corr}$  and MDT results for  $\Delta f = 0.6$  and  $\Delta f = 0.55$  indicate that peak  $\Delta_{corr}$  obtained from the EEG, ECoG, fMRI or etc., and the position where MDT of *Int* and *Seg* are equal, are close. This provides an anchor point between neurophysiological dynamics and thermodynamics, psychoacoustic data, and theoretical simulations. Furthermore, dynamic reconstruction of biological systems is gaining attention (90-92). With time sequence data, dynamics and thermodynamics can reveal phase transitions in biological systems.

**Attention model.** Initial auditory stream organization can also produce brief integrated dominance, resembling attention below baseline values (13, 16, 69). Since initial organization involves gradual attention increase, a constant baseline attention model may be overly simplistic. During experiments, we observed that the attention is naturally drawn to stimuli and shifts with perception changes subconsciously. Therefore, we propose an alternative explanation: Stochastic attention fluctuations by stimuli induction lead to perception alternation (Fig.7(b9-b12, b13-b16)). Besides, conscious attention modulation may not be restricted to the primary auditory

cortex as shown in Fig.1 but involve higher hierarchies. Nonetheless, it does not impact the dynamics from our original model.

**Noise coefficient  $D$  and presentation rate.** Noise is often interpreted as inherent to neural systems. However, Experiment I shows that longer tone duration or slower presentation rate leads to longer average *Int*-intermediation duration. This is not an isolated finding (14, 93). On the other hand, smaller  $D$  values create higher landscape barriers, increasing MDTs for all perceptions. The slower PR acts as the lower attention of two sides, resembling decreasing the  $D$  in the area of *Int* or increasing the  $D$  in the area of *Seg x* and *Seg y*. Meanwhile, some studies suggest that temporal relationships influence auditory streams (94, 95). Slower PR may disrupt temporal synchronization among neural pathways at specific frequencies, contributing to a noise-like effect. Furthermore, the fact that neural circuit dynamics produce some stable auditory perceptual states may relate to the auditory phase locking (96, 97).

**Almost coefficient-independent structural stability, and expansibility.** We additionally try to expanded or reduced the coefficients in the model by 50% based on the original values. The results manifest that changing  $k$  in  $F_{MGB}$ ,  $\gamma$  in  $F_{IC}$ , as well as  $\sigma$ ,  $\rho$ , and  $v$  in  $F(\Delta f)$  acting on the global neural pathway will alter the  $\Delta f$  range for achieving the entire dynamical phase transition process (Eq.(1, 3)). Changes in other coefficients (including ones in adaptation  $\Lambda(x)$ ,  $\Lambda(y)$ ) have almost no impact on the dynamics. Whereas, deleting or changing any connection in Fig.1(b) or adaptation result in a disparate global dynamics. Besides, this framework can accommodate more complicated situations through paralleling more cortex components that are mapped with different frequencies in the model. These results suggest once again that the holistic topological structure of neural pathways can reveal the foundation of brain perceptual functions.

## Materials and Methods

Eq.(3) represents an deterministic description about the firing rates of the cortical populations  $x$  and  $y$ . However, a biological system inherently possesses internal and external randomness. We adopt the external white noise  $\xi(t)$  with  $\langle \xi(t)\xi(t') \rangle = \delta(t-t')$  to approach the intricate fluctuation of ion concentration, the sensitivity of ion channel, etc., among the nerve cells. Thus, Eq.(3) develops into the general Langevin equations:

$$\begin{aligned}\frac{dx}{dt} &= F_1 + \sqrt{2D} \xi(t) \\ \frac{dy}{dt} &= F_2 + \sqrt{2D} \xi(t)\end{aligned}\tag{7}$$

where  $D$  is the constant and isotropic diffusion coefficient as the matrix elements  $D_{11} = D_{22}$  in diffusion matrix  $\mathbf{D}$ .

Eq.(7) reflect the stochastic dynamical behavior of the system. The Fokker-Planck equation can be derived from the stochastic differential equations Eq.(7):

$$\frac{\partial P(x, y, t)}{\partial t} = -\frac{\partial}{\partial x}(F_1 P) - \frac{\partial}{\partial y}(F_2 P) + D\left(\frac{\partial^2}{\partial x^2} + \frac{\partial^2}{\partial y^2}\right)P\tag{8}$$

Noting that the probability flux is

$$\mathbf{J} = \mathbf{F}P - \mathbf{D} \cdot \nabla P\tag{9}$$

Eq.(8) can be expressed in the form of  $\partial P/\partial t = -\nabla \cdot \mathbf{J}$ . This is a probability conservation law where the change of the probability is equal to the net flux in or out. When the system reaches nonequilibrium steady state, it reads  $0 = \nabla \cdot \mathbf{J}_{ss}$ , which indicates  $\mathbf{J}_{ss}$  fluxes constitute the rotational field. The non-zero flux  $\mathbf{J}_{ss}$  indicates that there is a net input or output flux. This breaks the detailed balance and leads the system to be in the intrinsic nonequilibrium state. Hence, the driving force at a certain position in the stochastic dynamics can be decomposed into the flux  $\mathbf{J}_{ss}$  and the landscape gradient therein as  $\mathbf{F} = \mathbf{J}_{ss}/P_{ss} - \mathbf{D} \cdot \nabla U$  in a view of probability, where

$$U = -\ln(P_{ss})\tag{10}$$

is the generalized potential landscape. These compose the foundation of the nonequilibrium physics methods.

**Dominant path** possesses a maximum probability among all the connecting paths between arbitrary two states in the system. This is a derived result from the path integral of stochastic dynamics (27, 28). Resembling

the well-known quantum path integral, it is critical to determine the effective Lagrangian, which is called Onsager-Machlup functional:

$$L_{OM} = \frac{1}{4D} [(\dot{x} - F_x)^2 + (\dot{y} - F_y)^2] + \frac{1}{2} \left( \frac{\partial F_x}{\partial x} + \frac{\partial F_y}{\partial y} \right) \quad (11)$$

Correspondingly, a certain path  $\mathcal{X}$  with time span  $[0, \tau]$  has the probability:

$$P[\mathcal{X}] = \exp\left(-\int_0^\tau L_{OM} dt\right) \quad (12)$$

Eq.(12), which belongs to two-points boundary value problem, is usually difficult to solve or seeking extreme value by Euler-Lagrange equation. However, based on the directly discretizing method of Onsager-Machlup functional (98-100), we employ genetic gradient annealing algorithm to seek the path that renders the integral in Eq.(12) to reach the minimal value.

**Average nonequilibrium flux** *ave*  $\mathbf{J}_{ss}$  can grasp the global thermodynamical property of the system, in terms of that  $\mathbf{J}_{ss}$  is the flow of global stable probability, meanwhile  $\mathbf{J}_{ss}$  is the main  $\mathbf{F}$  component of deflection in the case of multi-stabilities. The definition of *ave*  $\mathbf{J}_{ss}$  reads:

$$\int_{\Omega} P_{ss} |\mathbf{J}_{ss}|^2 d\Omega \quad \Omega \text{ is the domain of system} \quad (13)$$

Given that  $\mathbf{J}_{ss}$  features in the entropy production and the detailed balance breaking, the *ave*  $\mathbf{J}_{ss}$  is expected a consistent tendency with them.

**Rates of entropy production and heat dissipation** reflect the properties of nonequilibrium thermodynamics and energetics. The general statistical physical entropy of the system is  $S_{sys} = -k_B \int_{\Omega} P \ln(P) d\Omega$ . Considering the Einstein's relation  $D = k_B T$  and through some integral substitution, we have:

$$\begin{aligned} T\dot{S}_{sys} &= \int_{\Omega} |\mathbf{J}|^2 / P d\Omega - \int_{\Omega} \mathbf{F} \cdot \mathbf{J} d\Omega \\ &= T\dot{S}_{tot} - T\dot{S}_{env} \\ &= EPR - HDR \end{aligned} \quad (14)$$

where  $T\dot{S}_{tot}$  is the total *EPR* of the system and environment,  $T\dot{S}_{env}$  is the entropy change rate of the environment that equals to the heat dissipation rate (*HDR*) of the system, and  $T\dot{S}_{sys}$  is the entropy production rate of the system itself. . Note that the definition of *EPR* has the same dimension with power. In fact,  $T\dot{S}_{tot}$  represents the upper bound of the time change rate of the irreversible work applied to the system, while  $T\dot{S}_{env}$  represents the time change rate of heat exchange between the system and the environment (33, 34). When the system reaches stable state,  $\dot{S}_{sys} = 0$ , and  $EPR = HDR$ . Therefore, although it is usually infeasible to precisely define the energy of the system, we can still utilize the work and dissipation cost of the system. Note that *EPR* can be used as a measure of the thermodynamic cost or dissipation, and it is directly related to the nonequilibrium flux .

**Time irreversibility and degree of the detailed balance breaking** originates from the asymmetric flow  $\mathbf{J}_{ss}$  within the system. The difference between the forward and reverse cross-correlation:

$$\begin{aligned} \Delta_{corr} &= |\langle X(t) \cdot Y(t + \tau) \rangle - \langle Y(t) \cdot X(t + \tau) \rangle| \\ &= \left| \int_{\Omega} d\Omega \cdot [X^i P^i(t) Y^j P^j(t + \tau) w^{ij}(\tau) - Y^i P^i(t) X^j P^j(t + \tau) w^{ji}(\tau)] \right| \\ &\cong \left| \int_{\Omega} d\Omega \cdot XY\tau (J_X^{ij} + J_Y^{ij}) \right| \end{aligned} \quad (15)$$

is the effective statistical characteristic to measure the detailed balance breaking and time irreversibility, where  $w^{ij}(\tau)$  is the transition probability of state  $i$  transiting to state  $j$  during the interval  $\tau$  (35, 37). It precisely

quantifies the time asymmetry and non-zero flux between states among the entire system. The larger  $\Delta_{corr}$  is, the intenser the time irreversibility and detailed balance breaking are.

However, it is difficult to define  $\tau$  and calculate Eq.(15) among the global continuous system. Practically, we use long time average to substitute ensemble average. That is, for each set of  $D$  and  $\Delta f$ , the stochastic  $x, y$  sequences of 300000 time span are generated, and we calculate the difference between the time forward and backward cross-correlations of  $x, y$ . Then, this procedure is repeated for 300 times and averaged. Finally,  $\Delta_{corr}$  for a set of  $D$  and  $\Delta f$  is gained. As stressed in main content, simulation based on the finite sequence instead of the complicated integral has experimental practicality.

## Appendix

Here are the values of the coefficients in the model:

In  $\Lambda(x)$  and  $\Lambda(y)$ ,  $a = 0.85$ ,  $b = 0.15$ ,  $c = 5$ .

In  $F(\Delta f)$ ,  $v = 0.25$ .

In Eq.(1),  $g = 1$ ,  $\alpha = 1.4$ ,  $\beta = 0.028$ ,  $\eta = 0.02$ ,  $\gamma = 0.315$ ,  $n = 0.25$ ,  $\omega = 2$ . For  $F_{MGB}^x$  and  $F_{MGB}^y$ ,  $\theta = 0.0001$  and  $k = 0.2$ .

In Eq.(2),  $\theta_x = \theta_y = 4$ .

In Eq.(3),  $\sigma = 0.25$ ,  $\rho = 0.025$ .

## Acknowledgments

Yuxuan Wu thanks the beneficial discussion with Xiaochen Wang on attention mechanism and coefficient dependency of the model.

Yuxuan Wu and Xiaona Fang thank the supports from National Natural Science Foundation of China (No.12234019 and No.32171245).

## References

1. M. Axer, K. Amunts, Scale matters: The nested human connectome. *Science* **378**, 500-504 (2022).
2. J. H. Lee, Q. Liu, E. Dadgar-Kiani, Solving brain circuit function and dysfunction with computational modeling and optogenetic fMRI. *Science* **378**, 493-499 (2022).
3. M. Thiebaut de Schotten, S. J. Forkel, The emergent properties of the connected brain. *Science* **378**, 505-510 (2022).
4. M. G. Perich, K. Rajan, Rethinking brain-wide interactions through multi-region 'network of networks' models. *Current Opinion in Neurobiology* **65**, 146-151 (2020).
5. H. S. J. Cheong, I. Siwanowicz, G. M. Card, Multi-regional circuits underlying visually guided decision-making in Drosophila. *Current Opinion in Neurobiology* **65**, 77-87 (2020).
6. D. A. Leopold, N. K. Logothetis, Activity changes in early visual cortex reflect monkeys' percepts during binocular rivalry. *Nature* **379**, 549-553 (1996).
7. C. Mo, J. Lu, C. Shi, F. Fang, Neural representations of competing stimuli along the dorsal and ventral visual pathways during binocular rivalry. *Cereb. Cortex* **33**, 2734-2747 (2022).
8. J. D. Yao, P. Bremen, J. C. Middlebrooks, Emergence of Spatial Stream Segregation in the Ascending Auditory Pathway. *J. Neurosci.* **35**, 16199-16212 (2015).
9. B. AS, *Auditory scene analysis: The perceptual organization of sound* (MIT Press, 1990).
10. S. Haykin, Z. Chen, The Cocktail Party Problem. *Neural Computation* **17**, 1875-1902 (2005).
11. P. Sterzer, A. Kleinschmidt, G. Rees, The neural bases of multistable perception. *Trends in Cognitive Sciences* **13**, 310-318 (2009).
12. v. Noorden (1975) Temporal coherence in the perception of tone sequences. (Eindhoven University of Technology).
13. J. Rankin, E. Sussman, J. Rinzal, Neuromechanistic Model of Auditory Bistability. *PLoS Comput. Biol.* **11**, e1004555 (2015).

14. R. W. Mill, T. M. Bohm, A. Bendixen, I. Winkler, S. L. Denham, Modelling the Emergence and Dynamics of Perceptual Organisation in Auditory Streaming. *PLoS Comput. Biol.* **9**, 21 (2013).
15. I. Winkler, S. Denham, R. Mill, T. M. Bohm, A. Bendixen, Multistability in auditory stream segregation: a predictive coding view. *Philos. Trans. R. Soc. B-Biol. Sci.* **367**, 1001-1012 (2012).
16. B. C. J. Moore, H. E. Gockel, Properties of auditory stream formation. *Philosophical Transactions of the Royal Society B: Biological Science* **367**, 919–931 (2012).
17. D. Pressnitzer, J.-M. Hupé, Temporal Dynamics of Auditory and Visual Bistability Reveal Common Principles of Perceptual Organization. *Curr. Biol.* **16**, 1351-1357 (2006).
18. M. Elhilali, J. J. Xiang, S. A. Shamma, J. Z. Simon, Interaction between Attention and Bottom-Up Saliency Mediates the Representation of Foreground and Background in an Auditory Scene. *PLoS. Biol.* **7**, 14 (2009).
19. A. Byrne, J. Rinzel, J. Rankin, Auditory streaming and bistability paradigm extended to a dynamic environment. *Hearing Research* **383**, 12 (2019).
20. D. Chakrabarty, M. Elhilali, A Gestalt inference model for auditory scene segregation. *PLoS Comput. Biol.* **15**, 33 (2019).
21. S. N. Wrigley, G. J. Brown, A computational model of auditory selective attention. *IEEE Trans. Neural Netw.* **15**, 1151-1163 (2004).
22. Q. A. Nguyen, J. Rinzel, R. Curtu, Buildup and bistability in auditory streaming as an evidence accumulation process with saturation. *PLoS Comput. Biol.* **16**, 34 (2020).
23. A. Paredes-Gallardo, T. Dau, J. Marozeau, Auditory Stream Segregation Can Be Modeled by Neural Competition in Cochlear Implant Listeners. *Front. Comput. Neurosci.* **13** (2019).
24. D. L. Wang, Primitive auditory segregation based on oscillatory correlation. *Cogn. Sci.* **20**, 409-456 (1996).
25. G.W.Gardiner, *Handbook of Stochastic Methods* (Springer-Berlin, ed. 3, 2004).
26. J. Wang, Landscape and flux theory of non-equilibrium dynamical systems with application to biology. *Advances in Physics* **64**, 1-137 (2015).
27. H. S. Wio, *Path Integrals For Stochastic Processes: An Introduction* (World Scientific Publishing Co. Pte. Ltd., Singapore, ed. 1, 2013).
28. M. Chaichian, A. Demichev, *Path Integrals in Physics* (IOP Publishing, 2001), vol. I.
29. C. Howarth, P. Gleeson, D. Attwell, Updated energy budgets for neural computation in the neocortex and cerebellum. *J. Cereb. Blood Flow Metab.* **32**, 1222-1232 (2012).
30. M. W. H. Remme, J. Rinzel, S. Schreiber, Function and energy consumption constrain neuronal biophysics in a canonical computation: Coincidence detection. *PLoS Comput. Biol.* **14**, 20 (2018).
31. O. A. Zhukov, T. A. Kazakova, G. V. Maksimov, A. R. Brazhe, Cost of auditory sharpness: Model-Based estimate of energy use by auditory brainstem "octopus" neurons. *J. Theor. Biol.* **469**, 137-147 (2019).
32. L. Xu, D. Patterson, A. C. Staver, S. A. Levin, J. Wang, Unifying deterministic and stochastic ecological dynamics via a landscape-flux approach. *Proc. Natl. Acad. Sci. U. S. A.* **118**, 12 (2021).
33. K. Sekimoto, *Stochastic Energetics*, Lect. Notes. Phys (Springer, Berlin Heidelberg, 2010).
34. U. Seifert (2010) Stochastic thermodynamics: An introduction. in *11th Granada Seminar on Computational and Statistical Physics* (Amer Inst Physics, La Herradura, SPAIN), pp 56-76.
35. H. Qian, E. L. Elson, Fluorescence correlation spectroscopy with high-order and dual-color correlation to probe nonequilibrium steady states. *Proc. Natl. Acad. Sci. U. S. A.* **101**, 2828-2833 (2004).
36. K. Zhang, J. Wang, Exploring the Underlying Mechanisms of the *Xenopus laevis* Embryonic Cell Cycle. *J. Phys. Chem. B* **122**, 5487-5499 (2018).
37. F. Zhang, J. Wang, Nonequilibrium indicator for the onset of epileptic seizure. *Physical review. E* **108**, 044111 (2023).
38. J. S. Snyder, C. Alain, Toward a neurophysiological theory of auditory stream segregation. *Psychol. Bull.* **133**, 780-799 (2007).
39. A. H. Mehta, I. Yasin, A. J. Oxenham, S. Shamma, Neural correlates of attention and streaming in a perceptually multistable auditory illusion. *J. Acoust. Soc. Am.* **140**, 2225-2233 (2016).
40. E. S. Sussman, Auditory Scene Analysis: An Attention Perspective. *J. Speech Lang. Hear. Res.* **60**, 2989-3000 (2017).

41. J. Rankin, J. Rinzel, Attentional control via synaptic gain mechanisms in auditory streaming. *Brain Res.* **1778**, 12 (2022).
42. A. J. Billig, M. H. Davis, R. P. Carlyon, Neural Decoding of Bistable Sounds Reveals an Effect of Intention on Perceptual Organization. *J. Neurosci.* **38**, 2844-2853 (2018).
43. J. Pickles, *An Introduction to the Physiology of Hearing* (Brill, Leiden, ed. 4, 2012).
44. E. R. Kandel, J. D. Koester, S. H. Mack, S. A. SIEGELBAUM, *PRINCIPLES OF NEURAL SCIENCE* (McGraw Hill, ed. 6, 2021).
45. M. Ono, T. Ito, Inhibitory Neural Circuits in the Mammalian Auditory Midbrain. *J. Exp. Neurosci.* **12**, 11 (2018).
46. J. O. Pickles, Auditory pathways: anatomy and physiology. *Handbook of clinical neurology* **129**, 3-25 (2015).
47. A. M. H. Lesicko, M. N. Geffen, Diverse functions of the auditory cortico-collicular pathway. *Hearing Research* **425**, 108488 (2022).
48. C. C. Lee, Thalamic and cortical pathways supporting auditory processing. *Brain and Language* **126**, 22-28 (2013).
49. B. A. Nayagam, M. A. Muniak, D. K. Ryugo, The spiral ganglion: Connecting the peripheral and central auditory systems. *Hearing Research* **278**, 2-20 (2011).
50. D. A. X. Nayagam, J. C. Clarey, A. G. Paolini, Powerful, onset inhibition in the ventral nucleus of the lateral lemniscus. *J. Neurophysiol.* **94**, 1651-1654 (2005).
51. H. M. Zhang, J. B. Kelly, Responses of neurons in the rat's ventral nucleus of the lateral lemniscus to amplitude-modulated tones. *J. Neurophysiol.* **96**, 2905-2914 (2006).
52. S. Kuwada, D. C. Fitzpatrick, R. Batra, E. M. Ostapoff, Sensitivity to interaural time differences in the dorsal nucleus of the lateral lemniscus of the unanesthetized rabbit: Comparison with other structures. *J. Neurophysiol.* **95**, 1309-1322 (2006).
53. Y. Zhang, N. Suga, J. Yan, Corticofugal modulation of frequency processing in bat auditory system. *Nature* **387**, 900-903 (1997).
54. S. Da Costa, W. van der Zwaag, L. M. Miller, S. Clarke, M. Saenz, Tuning In to Sound: Frequency-Selective Attentional Filter in Human Primary Auditory Cortex. *J. Neurosci.* **33**, 1858-1863 (2013).
55. E. L. Bartlett, S. Sadagopan, X. Q. Wang, Fine frequency tuning in monkey auditory cortex and thalamus. *J. Neurophysiol.* **106**, 849-859 (2011).
56. L. I. Zhang, Y. Zhou, H. Z. W. Tao, Inhibitory synaptic mechanisms underlying functional diversity in auditory cortex. *J. Gen. Physiol.* **138**, 311-320 (2011).
57. R. Santoro *et al.*, Encoding of Natural Sounds at Multiple Spectral and Temporal Resolutions in the Human Auditory Cortex. *PLoS Comput. Biol.* **10**, 14 (2014).
58. A. Bidet-Caulet *et al.*, Effects of selective attention on the electrophysiological representation of concurrent sounds in the human auditory cortex. *J. Neurosci.* **27**, 9252-9261 (2007).
59. M. A. Merchan, P. Berbel, Anatomy of the ventral nucleus of the lateral lemniscus in rats: a nucleus with a concentric laminar organization. *The Journal of comparative neurology* **372**, 245-263 (1996).
60. M. S. Malmierca, T. B. Leergaard, V. M. Bajo, J. G. Bjaalie, M. A. Merchan, Anatomic evidence of a three-dimensional mosaic pattern of tonotopic organization in the ventral complex of the lateral lemniscus in cat. *The Journal of neuroscience : the official journal of the Society for Neuroscience* **18**, 10603-10618 (1998).
61. R. Curtu, X. Y. Wang, B. W. Brunton, K. V. Nourski, Neural Signatures of Auditory Perceptual Bistability Revealed by Large-Scale Human Intracranial Recordings. *J. Neurosci.* **39**, 6482-6497 (2019).
62. D. Pérez-González, M. Malmierca, Adaptation in the auditory system: an overview. *Frontiers in Integrative Neuroscience* **8** (2014).
63. O. J. Grusser, M. Hagner, On the history of deformation phosphenes and the idea of internal light generated in the eye for the purpose of vision. *Documenta ophthalmologica. Advances in ophthalmology* **74**, 57-85 (1990).
64. R. Kanai, L. Chaieb, A. Antal, V. Walsh, W. Paulus, Frequency-Dependent Electrical Stimulation of the Visual Cortex. *Curr. Biol.* **18**, 1839-1843 (2008).
65. R. Cusack, J. Deeks, G. Aikman, R. P. Carlyon, Effects of location, frequency region, and time course of selective attention on auditory scene analysis. *J. Exp. Psychol.-Hum. Percept. Perform.* **30**, 643-656 (2004).



66. R. Chen *et al.*, Regulation and prediction of multistable perception alternation. *Chaos, Solitons & Fractals* **172**, 113564 (2023).
67. S. Anstis, S. Saida, ADAPTATION TO AUDITORY STREAMING OF FREQUENCY-MODULATED TONES. *J. Exp. Psychol.-Hum. Percept. Perform.* **11**, 257-271 (1985).
68. S. L. Denham, I. Winkler, The role of predictive models in the formation of auditory streams. *J. Physiol.-Paris* **100**, 154-170 (2006).
69. S. Deike, P. Heil, M. Bockmann-Barthel, A. Brechmann, The build-up of auditory stream segregation: a different perspective. *Front. Psychol.* **3**, 7 (2012).
70. A. Bendixen, S. L. Denham, K. Gyimesi, I. Winkler, Regular patterns stabilize auditory streams. *The Journal of the Acoustical Society of America* **128**, 3658-3666 (2010).
71. M. Elhilali, L. Ma, C. Micheyl, A. J. Oxenham, S. A. Shamma, Temporal Coherence in the Perceptual Organization and Cortical Representation of Auditory Scenes. *Neuron* **61**, 317-329 (2009).
72. J. M. Hupe, D. Pressnitzer, The initial phase of auditory and visual scene analysis. *Philos. Trans. R. Soc. B-Biol. Sci.* **367**, 942-953 (2012).
73. W. J. M. LEVELT, NOTE ON THE DISTRIBUTION OF DOMINANCE TIMES IN BINOCULAR RIVALRY. *British Journal of Psychology* **58**, 143-145 (1967).
74. P. Walker, Stochastic properties of binocular rivalry alternations. *Percept. Psychophys.* **18**, 467-473 (1975).
75. Y. H. Zhou, J. B. Gao, K. D. White, I. Merk, K. Yao, Perceptual dominance time distributions in multistable visual perception. *Biol. Cybern.* **90**, 256-263 (2004).
76. E. Schrödinger, Zur theorie der fall-und steigversuche an teilchen mit brownscher bewegung. *Physikalische Zeitschrift* **16**, 289-295 (1915).
77. A. W. Marshall, I. Olkin, *Life Distributions: Structure of Nonparametric, Semiparametric, and Parametric Families* (Springer, 2007).
78. A. Dykstra *et al.*, Widespread Brain Areas Engaged during a Classical Auditory Streaming Task Revealed by Intracranial EEG. *Frontiers in Human Neuroscience* **5** (2011).
79. M. G. Woldorff *et al.*, Modulation of early sensory processing in human auditory cortex during auditory selective attention. *Proc. Natl. Acad. Sci. U. S. A.* **90**, 8722-8726 (1993).
80. C. Micheyl, B. Tian, R. P. Carlyon, J. P. Rauschecker, Perceptual organization of tone sequences in the auditory cortex of awake Macaques. *Neuron* **48**, 139-148 (2005).
81. E. Selezneva, A. Gorkin, E. Budinger, M. Brosch, Neuronal correlates of auditory streaming in the auditory cortex of behaving monkeys. *Eur. J. Neurosci.* **48**, 3234-3245 (2018).
82. C. E. Schreiner, J. A. Winer, Auditory cortex mapmaking: Principles, projections, and rasticity. *Neuron* **56**, 356-365 (2007).
83. R. P. Carlyon, R. Cusack, J. M. Foxtan, I. H. Robertson, Effects of attention and unilateral neglect on auditory stream segregation. *J. Exp. Psychol.-Hum. Percept. Perform.* **27**, 115-127 (2001).
84. Y. Liu *et al.*, Selective and divided attention modulates auditory-vocal integration in the processing of pitch feedback errors. *Eur. J. Neurosci.* **42**, 1895-1904 (2015).
85. A. Kumar Neupane, K. Gururaj, G. Mehta, S. K. Sinha, Effect of Repetition Rate on Speech Evoked Auditory Brainstem Response in Younger and Middle Aged Individuals. *Audiology research* **4**, 106 (2014).
86. N. C. Higgins *et al.*, Adaptation in the sensory cortex drives bistable switching during auditory stream segregation. *Neurosci. Conscious.* **2023**, 12 (2023).
87. H. Yan, K. Zhang, J. Wang, Physical mechanism of mind changes and tradeoffs among speed, accuracy, and energy cost in brain decision making: Landscape, flux, and path perspectives. *Chin. Phys. B* **25**, 20 (2016).
88. D. Attwell, S. B. Laughlin, An energy budget for signaling in the grey matter of the brain. *J. Cereb. Blood Flow Metab.* **21**, 1133-1145 (2001).
89. C. Howarth, C. M. Peppiatt-Wildman, D. Attwell, The energy use associated with neural computation in the cerebellum. *J. Cereb. Blood Flow Metab.* **30**, 403-414 (2010).
90. D. Durstewitz, G. Koppe, M. I. Thurm, Reconstructing computational system dynamics from neural data with recurrent neural networks. *Nat. Rev. Neurosci.* **24**, 693-710 (2023).
91. X. J. Qiu *et al.*, Mapping transcriptomic vector fields of single cells. *Cell* **185**, 690+ (2022).

92. L. Zhu, J. Wang, Quantifying landscape-flux via single-cell transcriptomics uncovers the underlying mechanism of cell cycle. *bioRxiv* 10.1101/2023.08.01.551525, 2023.2008.2001.551525 (2023).
93. Y. I. Fishman, D. H. Reser, J. C. Arezzo, M. Steinschneider, Neural correlates of auditory stream segregation in primary auditory cortex of the awake monkey (vol 151, pg 167, 2001). *Hearing Research* **155**, 183-183 (2001).
94. D. A. Engstrom, J. A. S. Kelso, T. Holroyd, Reaction-anticipation transitions in human perception-action patterns. *Hum. Mov. Sci.* **15**, 809-832 (1996).
95. A. Friberg, J. Sundberg, TIME DISCRIMINATION IN A MONOTONIC, ISOCHRONOUS SEQUENCE. *J. Acoust. Soc. Am.* **98**, 2524-2531 (1995).
96. T. Noda, R. Kanzaki, H. Takahashi, Stimulus Phase Locking of Cortical Oscillation for Auditory Stream Segregation in Rats. *Plos One* **8**, 14 (2013).
97. R. Gransier, M. Hofmann, A. van Wieringen, J. Wouters, Stimulus-evoked phase-locked activity along the human auditory pathway strongly varies across individuals. *Scientific Reports* **11**, 13 (2021).
98. T. F. Miller, C. Predescu, Sampling diffusive transition paths. *J. Chem. Phys.* **126**, 12 (2007).
99. J. Lee, I. H. Lee, I. Joung, J. Lee, B. R. Brooks, Finding multiple reaction pathways via global optimization of action. *Nat. Commun.* **8**, 8 (2017).
100. J. Lee, B. R. Brooks, Direct global optimization of Onsager-Machlup action using Action-CSA. *Chem. Phys.* **535**, 10 (2020).